13

Heat Transfer Enhancement in Microchannel Heat Sink Using Nanofluids

P. Gunnasegaran, N.H. Shuaib, H.A. Mohammed,
M.F. Abdul Jalal and E. Sandhita
Department of Mechanical Engineering, College of Engineering
Universiti Tenaga Nasional, Km7
Jalan Kajang-Puchong, Selangor
Malaysia

1. Introduction

1.1 Introduction to microchannel heat sink (MCHS)

The microchannel heat sink (MCHS) cooling concept is first proposed by Tuckerman and Pease [1] in 1981. MCHSs are the most common and cost-effective hardware employed for the thermal management of MEMS devices. Tuckerman and Pease [1] pointed out that decreasing liquid cooling channel dimensions to the micron scale will lead to increase the heat transfer rate. They demonstrated experimentally a forty-fold improvement in heat-sinking capability in Si-base microchannels anodically bonded to Pyrex cover plates. Since then, intense research on MCHS have been conducted to study the heat transfer and fluid flow characteristics of MCHS.

There are two main configurations for the application of microchannel cooling which are direct cooling and indirect cooling. Direct cooling requires a direct contact between the surface to be cooled and the coolant fluid as illustrated in Fig.1.1a. This scheme reduces the thermal resistance between the surface and the coolant and thus, enhances the cooling effectiveness. However, electrical and chemical compatibility between the coolant and device itself needs to be ensured for this system to work [2]. An alternative to the above configuration is the use of a metallic heat sink to conduct the heat away from the device to a coolant which is forced through circular or noncircular grooves in the heat sink. Such an indirect cooling configuration shown in Fig.1.1b allows for a greater flexibility in coolant selection at the cost of increased thermal resistance between the device and the heat sink due to the heat diffusion resistance in the heat sink itself [3].

Microchannels are very fine channels of the width of a normal human hair and are widely used for electronic cooling purposes. In a MCHS, multiple microchannels are stacked together as shown in Fig.1.1 (b) which can increase the total contact surface area for heat transfer enhancement and reduce the total pressure drop by dividing the flow among many channels. Liquid or gas is used as a coolant to flow through these microchannels. The large surface area of MCHS enables the coolant to take away large amounts of energy per unit time per unit area while maintaining a considerably low device temperature. Using these MCHS, heat fluxes can be dissipated at relatively low surface temperatures.

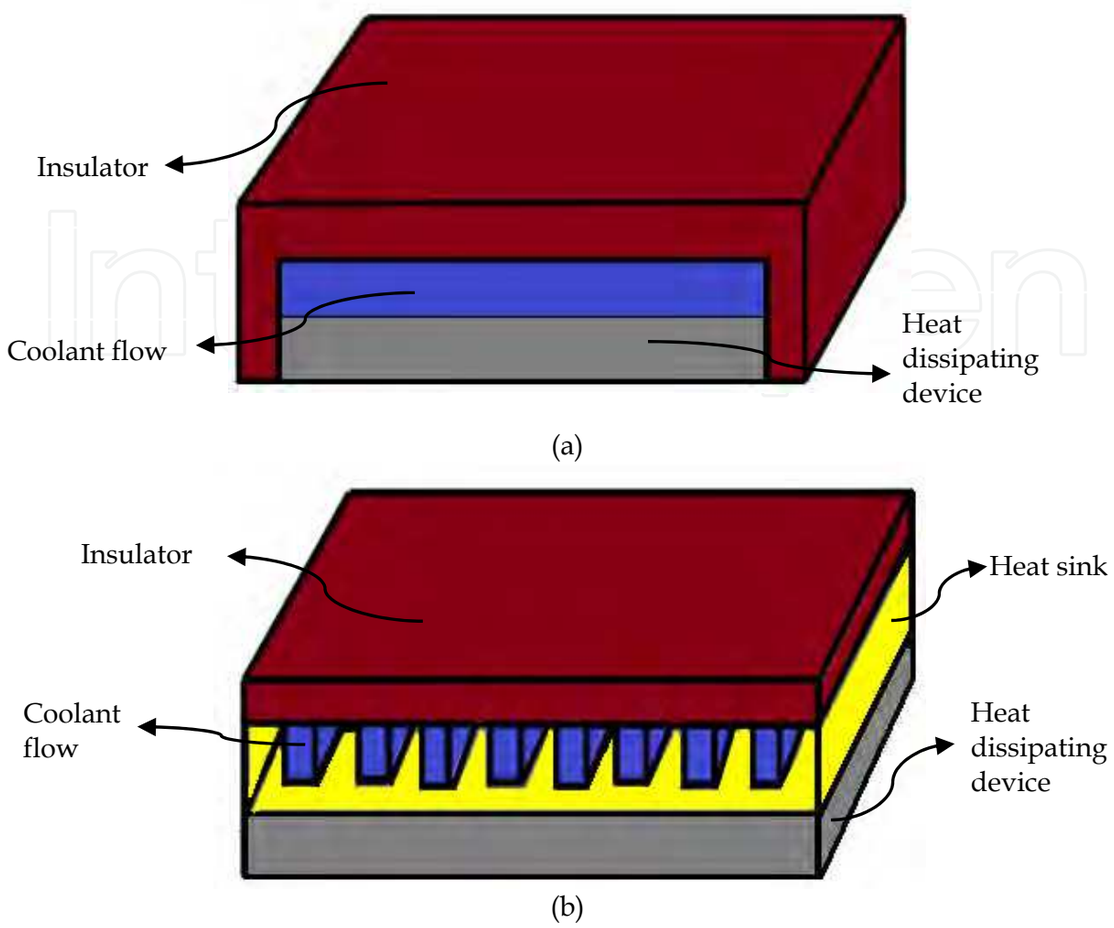

Fig. 1. Schematic diagram of the (a) direct cooling and (b) indirect cooling.

1.2 Cooling performance of MCHS

In order to drive the development of compact and efficient thermal management technology for advanced electronic devices, cooling devices have to be in light-weight, small in size and of high performance. Steinke and Kandlikar [4] presented a comprehensive review of friction factor data in microchannels with liquid flows. They indicated that entrance and exit losses need to be accounted for while presenting overall friction factors losses in microchannels. Most of the data that accounted for friction factor loss show good agreement with the conventional theory. They also provided a new procedure for correcting measured pressure drop to account for inlet and outlet losses.

Furthermore, three-dimensional fluid flow and heat transfer phenomena inside heated microchannels were investigated by Toh et al. [5]. They solved the steady laminar flow and heat transfer equations using a finite-volume method. It was found that the heat input lowers the frictional losses and viscosity leading to an increase in the temperature of the water, particularly at lower Reynolds numbers. Peng and Peterson [6,7] performed experimental investigations on the pressure drop and convective heat transfer of water flow in rectangular microchannels. They found that the cross sectional aspect ratio had a great influence on the flow friction and convective heat transfer both in laminar and

turbulent flows. Tiselj et al. [8] performed experimental and numerical analysis of the effect of axial conduction on the heat transfer in triangular microchannel heat sink. They pointed out that the bulk water and heated wall temperatures did not change linearly along the channel.

Inspired by the MCHS idea, new designs and modeling approaches of high performance cooling devices have been proposed, including using nanofluids as coolants in the MCHS study. Nanofluids are produced by dispersing nanometer-scale solid particles into base liquids such as water, ethylene glycol (EG), oils, etc. Lee et al. [9] used 38.4 nm of Al_2O_3 and 23.6 nm of CuO particles to enhance the thermal conductivity of water and EG. They showed that the enhancement percentage in thermal conductivity was not only a function of concentration and conductivities of the particles material and liquid, but it is also function of particle size and shape. Koo and Kleinstreuer [10] considered nanofluid flow in a representative microchannel, and conduction–convection heat transfer for different base fluids such as water and ethylene glycol with 20 nm CuO-nanoparticles. They come out with several suggestions which are a base fluid of high-Prandtl number such as ethylene glycol and oil should be used, using nanoparticles with high thermal conductivity are more advantageous, and a channel with high aspect ratio is desirable.

Chein and Huang [11] analyzed silicon microchannel heat sinks performance using nanofluids with a mixture of pure water and nanoscale Cu particles as coolants with various volume fractions. The MCHS with two specific geometries, one with W_{ch}=100 μm and L_{ch}=300 μm, the other with W_{ch}=57 μm and L_{ch}=365 μm, were examined. They found that the performances were greatly improved for these two specific geometries by using nanofluids as the coolants compared with pure water due to the increase in thermal conductivity of coolant and the nanoparticles thermal dispersion effect. The effectiveness of nanofluids for single-phase and two-phase heat transfer in microchannels is analyzed by Lee and Mudawar [12]. They indicated that the higher single-phase heat transfer coefficients are achieved in the entrance region of microchannels with increased nanoparticle concentration. However, the enhancement is weaker in the fully developed region. They suggested that nanoparticles should not be used in two-phase MCHS. This is because once boiling commences, particles begin to deposit into relatively large clusters near the channel exit due to localized evaporation. This clustering phenomenon quickly propagates upstream to fill the entire channel, preventing coolant from entering the heat sink and causing catastrophic failure of the cooling system. Jang and Choi [13] analyzed numerically the cooling performance of MCHS with nanofluids. They showed that the cooling performance of a MCHS with water-base nanofluids containing diamond (1%, 2 nm) at fixed pumping power of 2.25W was enhanced by about 10% compared with that of a MCHS with water.

There have been relatively few recent studies on nanofluid flow and heat transfer characteristics as comparing with those of pure fluid [14–16]. These studies showed that the heat transfer coefficient was greatly enhanced using nanofluid compared with pure fluid although there is a slight increase in pressure drop due to the presence of nanoparticles in MCHS operation. The enhancement depended on Reynolds number, particle volume fraction, and particle size and shape. It should be noted from the above literature review, however, that limited studies are available on nanofluid flow and heat transfer characteristics of rectangular shaped MCHS performance and this has motivated the present study.

The current study mainly focuses on 3D computational simulation of heat transfer and laminar liquid flow characteristics in MCHS. Following this introduction section, the governing equations and numerical model is explained, followed by studies on the geometrical parameters with various MCHS shapes (Section 3), effects of different nanoparticle volume fractions (Section 4), effects of different nanofluids types (Section 5), and effects of nanoparticle in different base fluids (Section 6).

2. Problem description and methodology

2.1 MCHS model

The physical configuration of the MCHS is schematically shown in Fig.2.1. The heat supplied to the MCHS substrate through a top plate is removed by flowing fluid through a number of 25 microchannels. This article focuses on heat transfer and liquid flow in three different cross sectional shapes of MCHS including rectangular, trapezoidal, and triangular. The dimensions of three different sets for each cross sectional shape of MCHS are given in Table 2.1-2.3.

	Case 1	Case 2	Case 3
H_{ch} (μm)	460	430	390
W_{ch} (μm)	180	280	380
L_c (μm)	10000	10000	10000
S (μm)	596	500	404
D_h (μm)	259	339	385
Number of channels	25	25	25

Table 2.1. Dimensions for three different sets of rectangular cross-section MCHS.

	Case 1	Case 2	Case 3
a (μm)	180	280	380
b (μm)	125	225	325
c (μm)	461	431	391
h (μm)	460	430	390
L_c (μm)	10000	10000	10000
S (μm)	596	500	404
D_h (μm)	229	318	370
Number of channels	25	25	25

Table 2.2. Dimensions for three different sets of trapezoidal cross-section MCHS.

	Case 1	Case 2	Case 3
k (μm)	180	280	380
l (μm)	469	452	434
h (μm)	460	430	390
L_c(μm)	10000	10000	10000
S (μm)	596	500	404
D_h (μm)	148	203	238
β	22.14°	36.07°	51.95°
Number of channels	25	25	25

Table 2.3. Dimensions for three different sets of triangular cross-section MCHS.

2.2 Governing equations

In the analysis of the entire domain of MCHS, it is necessary to set up the governing equations (continuity, momentum, and energy). For the specific case of heated flow through microchannels, the governing equations are solved with the following assumptions:

1. Both fluid flow and heat transfer are in steady-state and three-dimensional.
2. Fluid is in single phase, incompressible and the flow is laminar.
3. Properties of both fluid and heat sink material are temperature-independent.
4. All the surfaces of MCHS exposed to the surroundings are assumed to be insulated except the top plate where constant heat flux boundary condition, simulating the heat generation from electronic chip, is specified.

Thus, the governing equations in dimensionless form which are used in present study for heated MCHS can be written as [17]:

Continuity

$$\frac{\partial U}{\partial X}+\frac{\partial V}{\partial Y}+\frac{\partial W}{\partial Z}=0 \tag{2.1}$$

Momentum

X-Momentum: $$\left(U\frac{\partial U}{\partial X}+V\frac{\partial U}{\partial Y}+W\frac{\partial U}{\partial Z}\right)=-\frac{d\hat{P}}{dX}+\frac{1}{\mathrm{Re}}\left(\frac{\partial^2 U}{\partial X^2}+\frac{\partial^2 U}{\partial Y^2}+\frac{\partial^2 U}{\partial Z^2}\right) \tag{2.2a}$$

Y-Momentum: $$\left(U\frac{\partial V}{\partial X}+V\frac{\partial V}{\partial Y}+W\frac{\partial V}{\partial Z}\right)=-\frac{d\hat{P}}{dY}+\frac{1}{\mathrm{Re}}\left(\frac{\partial^2 V}{\partial X^2}+\frac{\partial^2 V}{\partial Y^2}+\frac{\partial^2 V}{\partial Z^2}\right) \tag{2.2b}$$

Z-Momentum: $$\left(U\frac{\partial W}{\partial X}+V\frac{\partial W}{\partial Y}+W\frac{\partial W}{\partial Z}\right)=-\frac{d\hat{P}}{dZ}+\frac{1}{\mathrm{Re}}\left(\frac{\partial^2 W}{\partial X^2}+\frac{\partial^2 W}{\partial Y^2}+\frac{\partial^2 W}{\partial Z^2}\right) \tag{2.2c}$$

Energy:

$$\left(U\frac{\partial \theta}{\partial X}+V\frac{\partial \theta}{\partial Y}+W\frac{\partial \theta}{\partial Z}\right)=\frac{1}{\mathrm{Re}.\mathrm{Pr}}\left(\frac{\partial^2 \theta}{\partial X^2}+\frac{\partial^2 \theta}{\partial Y^2}+\frac{\partial^2 \theta}{\partial Z^2}\right) \tag{2.3}$$

Where $X = \frac{x}{D_h}$, $Y = \frac{y}{D_h}$, $Z = \frac{z}{D_h}$, $U = \frac{u}{u_{in}}$, $V = \frac{v}{u_{in}}$, $W = \frac{w}{u_{in}}$, $\hat{P} = \frac{\Delta P}{\rho u_{in}^2}$ is the dimensionless pressure, and $\theta = \frac{T_f - T_i}{T_w - T_i}$ is the dimensionless temperature.

Given the complexity of these equations, computational methods of solving them are required. The methodology used in the present study to solve these governing equations is described in the following section.

2.3 Boundary conditions

Boundary conditions for all boundaries are specified for this simplified computational domain. Fig.2.1a shows the general MCHS computational model used in this study and Fig.2.1b shows the cross sectional shapes of channel considered in the study. Heat, supplied to the aluminum substrate through a top plate, is removed by flowing fluid through a number of microchannels.

At the entrance of the MCHS assembly (z = 0, from Fig.3.4a), two types of boundaries are encountered which are water flows through the microchannels and removes heat conducted to the surface of the MCHS. The remainder of the entrance is occupied by the aluminum substrate.

At the microchannels sections, the inlet fluid temperature was taken as 293K and the inlet fluid velocity was calculated using

$$u_{in} = \frac{\mathrm{Re}\,\mu}{\rho D_h} \tag{2.4}$$

For rectangular cross-section MCHS,

$$D_h = \frac{4A}{P} = \frac{2H_{ch}W_{ch}}{H_{ch} + W_{ch}} \tag{2.5a}$$

where A is the channel flow area, P is the channel wet perimeter, H_{ch} is the channel height, and W_{ch} is the channel width.

For trapezoidal cross-section MCHS,

$$D_h = \frac{4A}{P} = \frac{2(a+b)h}{a+b+2c} \tag{2.5b}$$

where A is the channel flow area, P is the channel wet perimeter, a is the channel top width, b is the channel bottom width, c is the channel hypotenuse, and h is the channel height.

For triangular cross-section MCHS,

$$D_h = \frac{4A}{P} = \frac{2kh}{k+2l} \tag{2.5c}$$

where A is the channel flow area, P is the channel wet perimeter, k is the channel width, h is the channel height, and l is the channel hypotenuse.

The Reynolds number in this work was ranged from 100 to 1000. In calculating the velocity, the fluid is assumed to be evenly distributed into all microchannels. The transverse velocities at the inlet are assumed to be zero. On the aluminum substrate, the velocities are zero, and it is assumed to be an adiabatic surface.

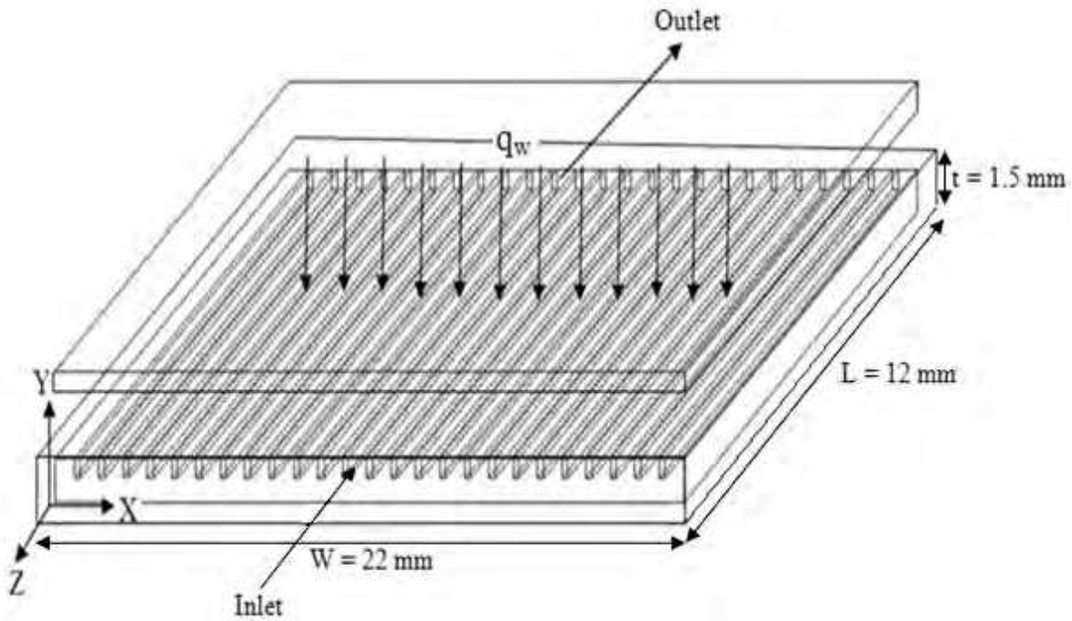

(a)

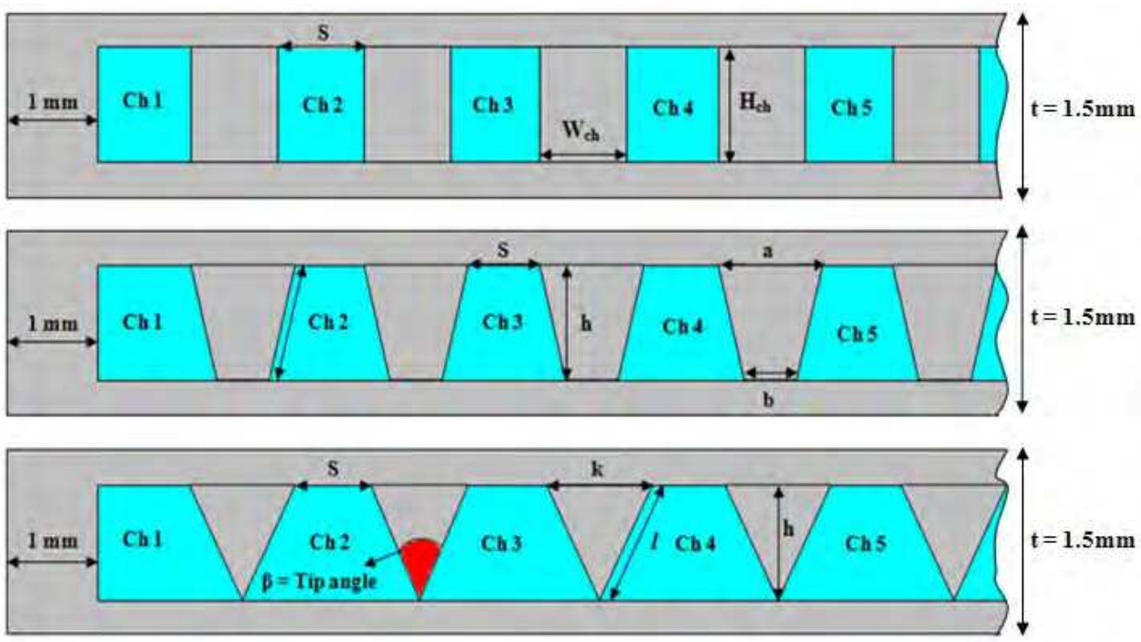

(b)

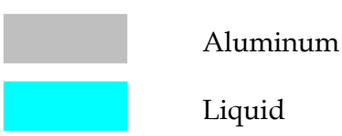

Fig. 2.1. (a) Schematic diagram of the MCHS (b) Section of the MCHS cross sectional shapes with its dimensions.

Boundary conditions at the inlet:

$$U = \frac{u}{u_{in}},\ U = 1,\ \theta = 1 \tag{2.6a}$$

At the outlet:

$$P = P_{out},\ \frac{\partial \theta}{\partial n} = 0 \tag{2.6b}$$

At the fluid-solid interface:

$$U = 0,\ \theta = \theta_s,\ -\kappa_s \frac{\partial \theta_s}{\partial n} = -\kappa \frac{\partial \theta}{\partial n} \tag{2.6c}$$

At the top plate:

$$q_w = -\kappa_s \frac{\partial \theta_s}{\partial n} \tag{2.6d}$$

In Eq. (2.6), U and θ are the dimensionless fluid inlet velocity and dimensionless temperature, respectively, P is the dimensionless pressure at the outlet, n is the direction normal to the wall or the outlet plane, and q_w is the heat flux applied at the top plate of the heat sink. The heat flux applied at the top plate was ranged from 100-1000 W/m^2.

2.4 Numerical solution using FVM

The governing conservation equations Eqs. (2) – (4) with the corresponding boundary conditions and equations for solid and fluid phases are simultaneously solved as a single domain conjugate problem using the standard finite volume method (FVM) with a hybrid differencing scheme [17]. The standard SIMPLE algorithm is used as the computational algorithm [18]. The iterations are continued until the sum of residuals for all computational cells became negligible (less than 10^{-7}) and velocity magnitudes did not change from iteration to iteration. Because of the assumption of constant fluid properties and negligible buoyancy, the mass and momentum equations are not coupled to the energy equation. Therefore, the temperature field is calculated by solving the energy equation after a converged solution for the flow field is obtained by solving the momentum and continuity equations.

2.5 Numerical implementation, grid testing and code validation

The distribution of hexahedral cells in the computational domain is determined from a series of tests with different number of cells. For example, for the case of rectangular MCHS, computational cells with 1.9x 10^5, 2.8 x 10^5, and 3.4 x 10^5 grids are used to test the grid independence of the solution. The results are shown in Figs.2.2 and 2.3 which present the dimensionless temperature profiles and dimensionless pressure drop across the heat sink versus Reynolds number, respectively. The dimensionless temperature and dimensionless pressure are defined in Eq.3.1(Section 3) and Eq.5.1(Section 5), respectively. It can be seen that almost identical results obtained when 2.8 x 10^5 and 3.4 x 10^5 grids are used. Thus, based on the results shown in these figures, a computational cell with 2.8 x 10^5 grids is employed for all the numerical computations in this study. Similar study was carried out for other MCHS shapes.

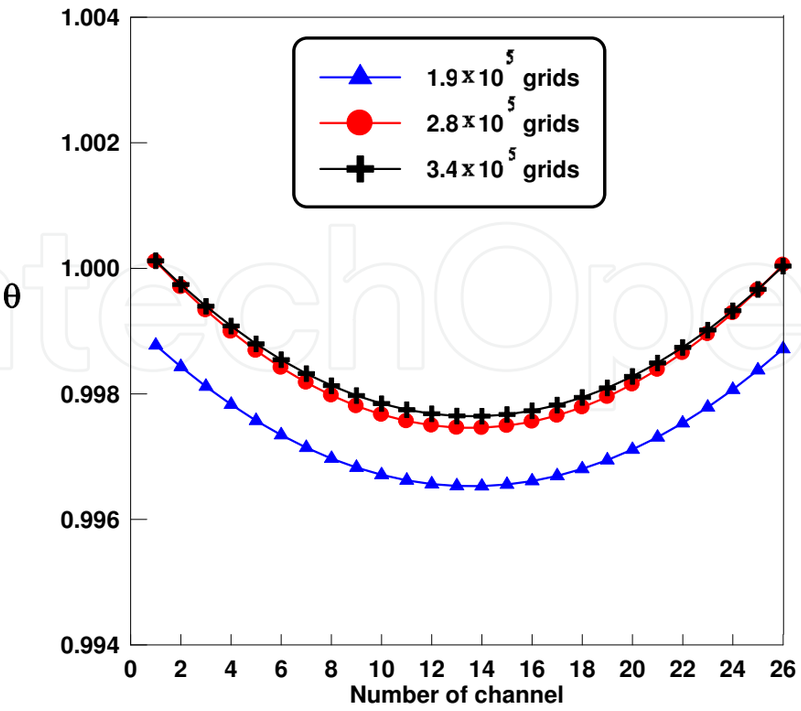

Fig. 2.2. Dimensionless temperature profiles for each channel in rectangular cross-section MCHS (D_h = 0.259 mm) using three different grids.

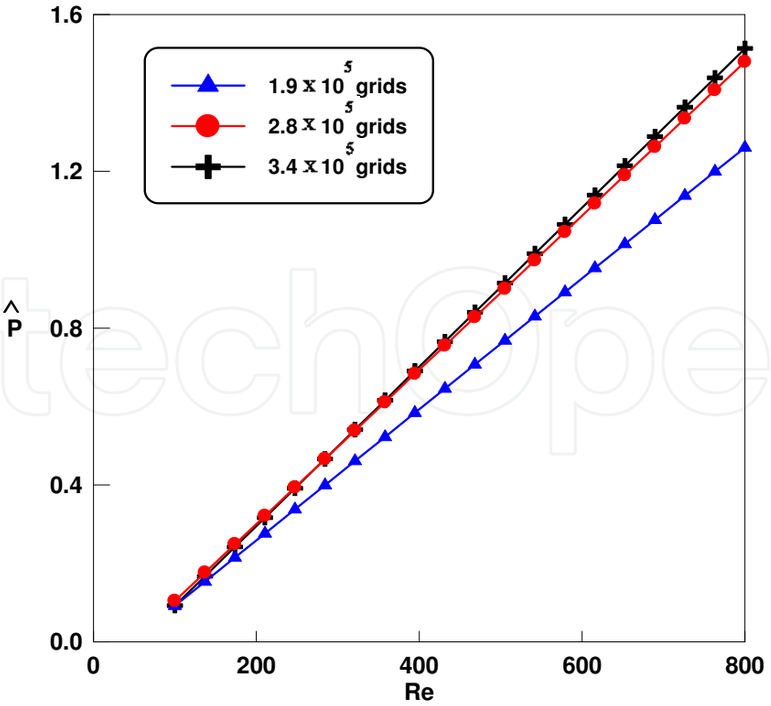

Fig. 2.3. Dimensionless pressure drop versus Reynolds number across the rectangular cross-section MCHS (D_h = 0.259 mm) using three different grids.

3. Effect of geometrical parameters of various MCHS shapes

This section investigates the effect of geometrical parameters on heat transfer and fluid flow characteristics for different cross sectional shapes of MCHS including rectangular, trapezoidal, and triangular with the dimensions as stated in Table 2.1-2.3, respectively. For this Section, water is used as the working fluid as the main aim is to investigate on the geometrical effects. For Section 4, 5, and 6, various nanofluids are used as the working fluid and only one particular cross sectional shape of MCHS with specified dimensions is considered for each Section. The dimensionless temperature profiles, heat transfer coefficient, friction factor, and thermal resistance which affected by geometrical parameters are discussed and presented.

3.1 Temperature profile

In the MCHS operation, the high temperature region should occur at the edge of the MCHS since there is no heat dissipation by fluid convection while the low-temperature region should occur in the region where microchannels are placed, especially at the middle regions of the MCHS due to the high heat transfer coefficient. To address this point, the dimensionless average temperature profiles of rectangular cross-section MCHS for different dimensions of the channel area at Re = 500 are presented in Fig.3.1. The dimensionless temperatures for each channel can be defined as:

$$\theta = \frac{T_f - T_i}{T_w - T_i} \tag{3.1}$$

Where T_f is the fluid temperature, T_i is the inlet temperature, and T_w is the wall temperature. It can clearly be seen from Fig.3.1 that the lower temperature profile occurs in the channels

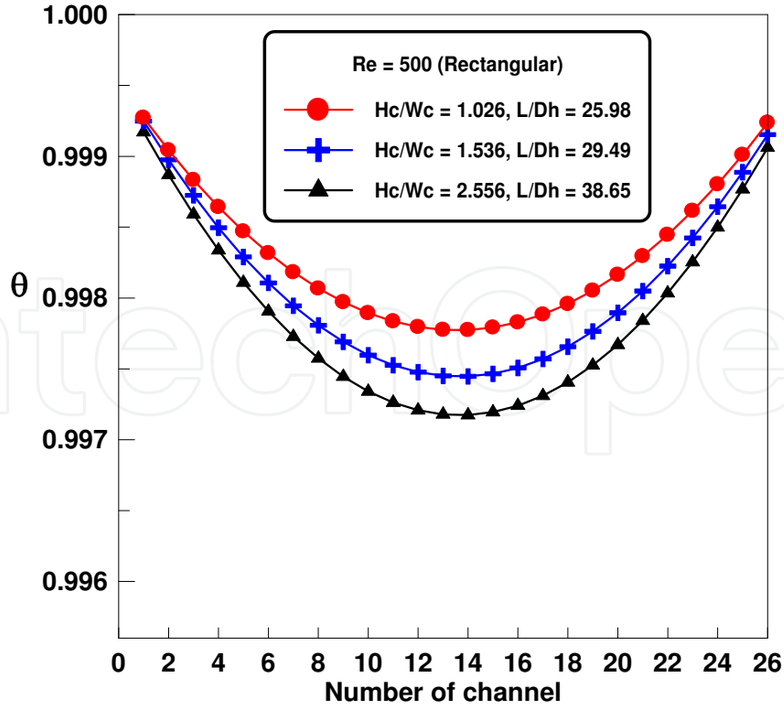

Fig. 3.1. Dimensionless average temperature profiles for each channel in rectangular cross-section MCHS.

located near the center of the MCHS. The validity of present result shows a similar trend with the result obtained by Chein and Chen [19]. For fluid in channels close to the edge of the MCHS, higher temperature profiles are observed due to the high heat transfer from the high-temperature edge of the MCHS.

3.2 Heat transfer coefficient

The computed averaged heat transfer coefficient in each channel of the rectangular cross-section MCHS for various hydraulic diameters is illustrated in Fig.3.2. The magnitude of heat transfer coefficient decreases with the increase in hydraulic diameter and the trends are the same for each cross sectional shape of the MCHS. This is due to the fact that lower pressure drop in larger hydraulic diameter corresponds to lower inlet velocity driven into the MCHS. Furthermore, due to the difference of the channel hydraulic diameter which is caused by the difference of channels' area and perimeter, the averaged heat transfer coefficient in each MCHS is also different under a given inlet velocity. For each type of the MCHS, the middle channel (channel number 14) has the highest averaged heat transfer coefficient value as expected. The averaged heat transfer coefficient value for other channels is seen to decrease depending on their distances from the wall. The averaged heat transfer coefficient distribution for all types of MCHS is almost symmetrical with respect to the centerline of the MCHS. It is shown that the heat transfer coefficient of the MCHS is greatly influenced by the hydraulic diameter of the channel, as the hydraulic diameter decreases, the heat transfer coefficient increases.

The computed average heat transfer coefficient versus Reynolds number for different cross sectional shapes of the MCHS is presented in Fig.3.3. It is apparent from this figure that the

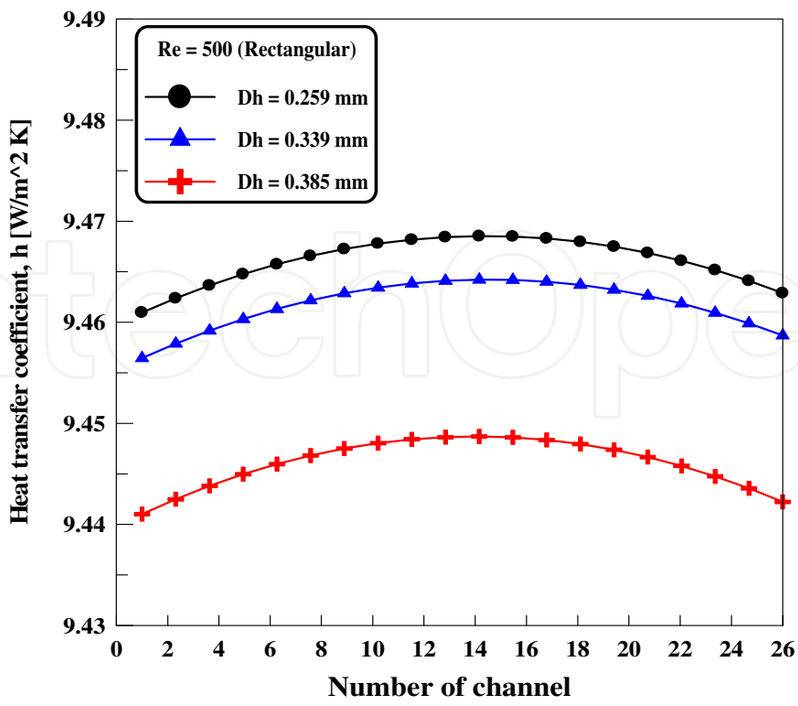

Fig. 3.2. Averaged heat transfer coefficient in each channel of the MCHS.

heat transfer coefficient for rectangular cross-section MCHS is the highest. The MCHS of triangular cross-section exhibits the lowest values of heat transfer coefficient. While, the heat transfer coefficient for trapezoidal cross- section MCHS is in between the rectangular and triangular.

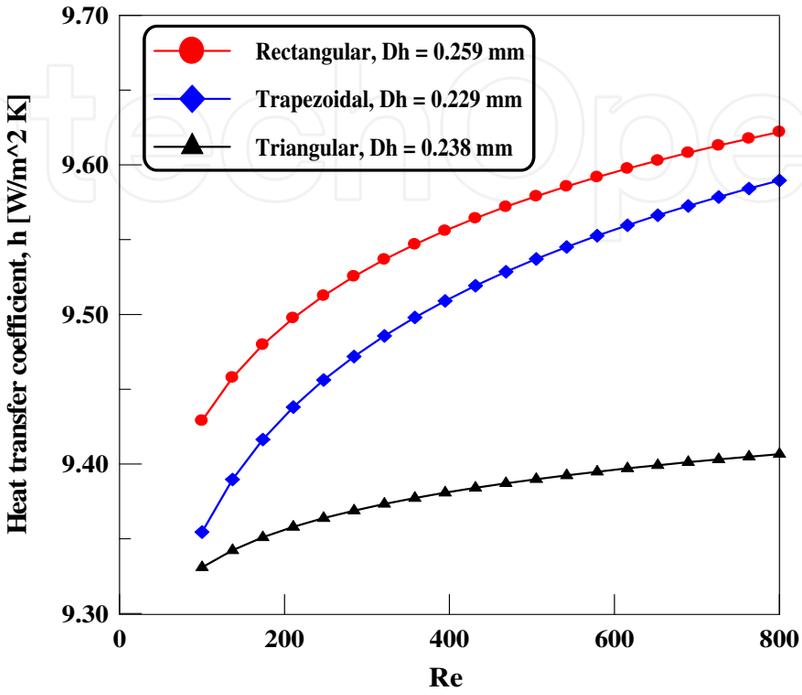

Fig. 3.3. Averaged heat transfer coefficient for different cross sectional shapes of the MCHS.

3.3 Friction factor

The effect of geometrical parameters on the friction factor, f for different microchannel shapes is discussed in this section. For the current study, the friction factor is calculated using Darcy equation [20]:

$$f = \frac{2D_h \, \Delta p}{\rho \, u_{in}^2 \, L_c} \tag{3.2}$$

Where D_h is the hydraulic diameter, Δp is the pressure drop, ρ is the density of water, u_{in} is the inlet velocity of water, and L_c is the length of channel.

Fig.3.4 shows the friction factor, f, at different W_c/H_c ratios for rectangular cross-section MCHS. It is clearly observed that f increases with the increase of W_c/H_c ratio of the channel. Therefore, the flow resistance will increase evidently when the ratio is increased. The reason behind this is that the increase in W_c/H_c ratio causes a decrease in the flow area and the pressure drop becomes significant. The validity of the present numerical results was also approved by Kandlikar et al. [21] results, where f increases with the increase of W_c/H_c ratio for rectangular cross-section MCHS.

Fig.3.5 shows f with three geometrical parameters including bottom-to-top width ratio *(b/a)*, height-to-top width ratio *(h/a)*, and length-to-hydraulic diameter ratio *(L/D_h)*, which affect the friction and heat transfer in the trapezoidal cross-section MCHS. Fig.3.6 shows a comparison of predicted Poiseuille number which is the product of friction factor, f and

Reynolds number, *fRe* from the present numerical simulation for trapezoidal cross-section MCHS with the experimental work done by Wu and Cheng [22]. As noticed, a very good agreement is obtained between the two studies whereby it is shown that *fRe* rises with the increase of Reynolds number. As can be noticed from Fig.3.6, *fRe* increases linearly with the increase of Reynolds number due to the linear dependency of pressure drop on constant inlet velocity for a fixed hydraulic diameter in fully developed laminar region. Thus, *fRe* is linearly proportional to Reynolds number for fully developed channel flow.

The *f* with different tip angles of triangular cross-section MCHS is illustrated in Fig.3.7. It is clearly observed that *f* increases with the increases of tip angle of the channel. The validity of the present numerical simulation result was also approved by the results of Kandlikar et al. [21]. The results show that the flow behavior is very similar for all types of cross sectional shapes of MCHS where the friction factor decreases with the increase of Reynolds number.

In overall, From the Figs.3.4, 3.5, and 3.7, it is also apparent that *f* for rectangular shaped microchannel is most, for trapezoidal shaped microchannel is less, and for triangular shaped microchannel is least. This is due to the triangular shaped microchannel has a smallest area. For trapezoidal shaped microchannels, the flow area is changed suddenly from larger area to smaller area, thus the pressure drop would be large. Therefore, *f* value for trapezoidal shaped microchannels is also larger than the triangular shaped microchannels. For the rectangular shaped microchannels, the flow area is the largest which corresponds to the highest value of *f*. Therefore, *f* of water flowing in MCHS, having the same width and height but with different cross sectional shapes can be very much different due to the difference of the cross sectional shape and geometrical dimensions of the channels.

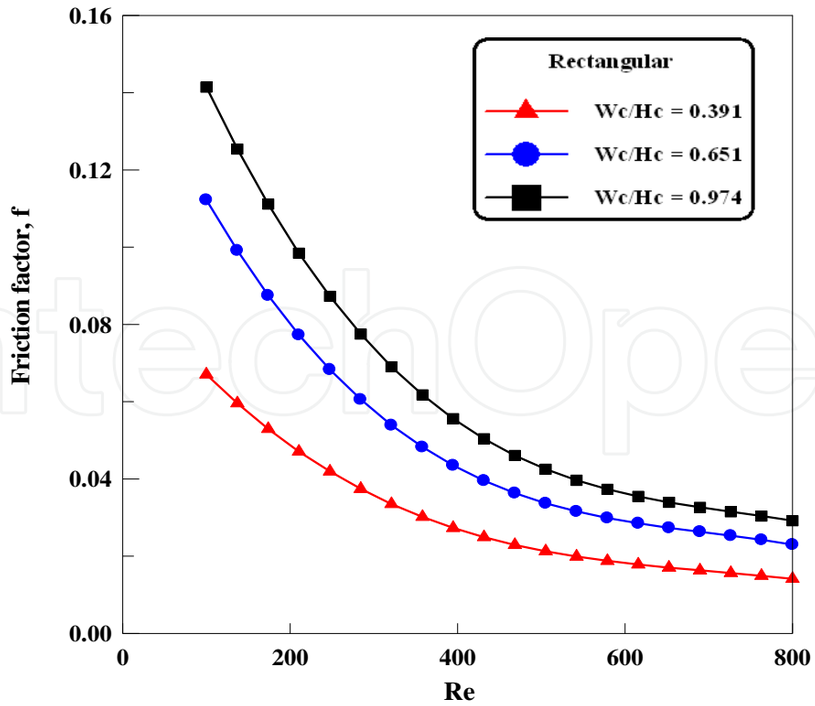

Fig. 3.4. Friction factor at different width-height (W_c/H_c) ratio for rectangular cross-section MCHS.

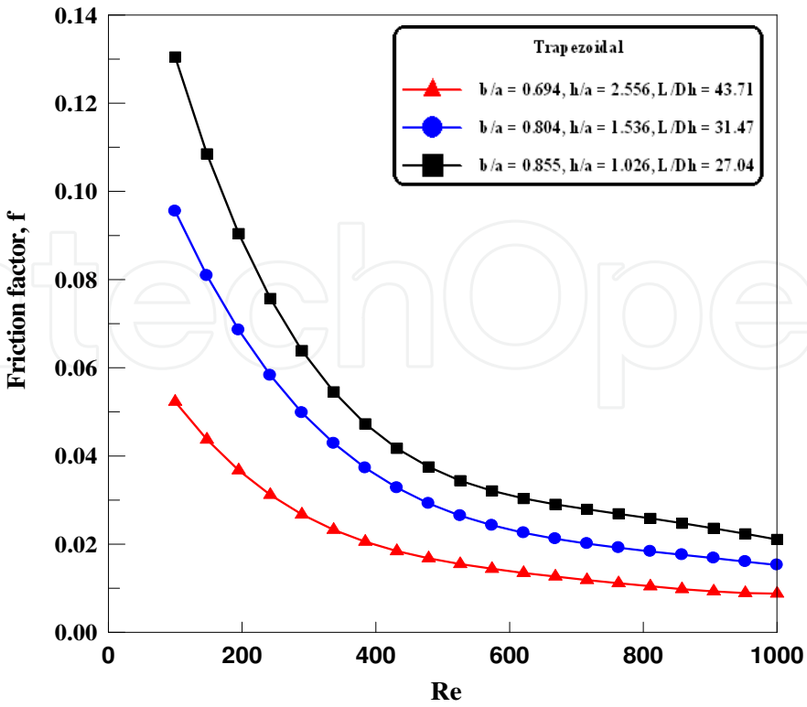

Fig. 3.5. Friction factor with three different geometrical parameters of trapezoidal cross-section MCHS.

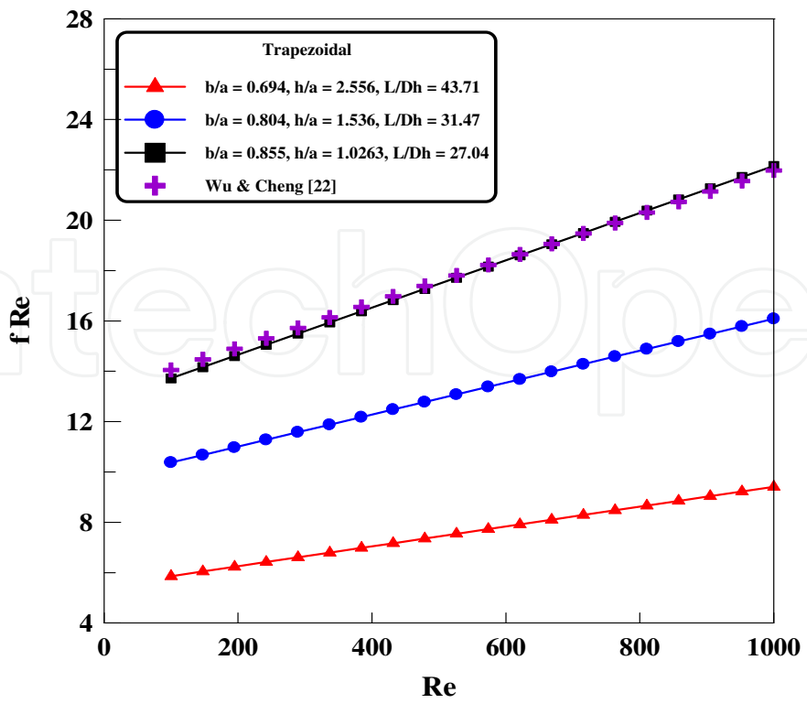

Fig. 3.6. Comparison of Poiseuille number of trapezoidal cross-section MCHS with [22].

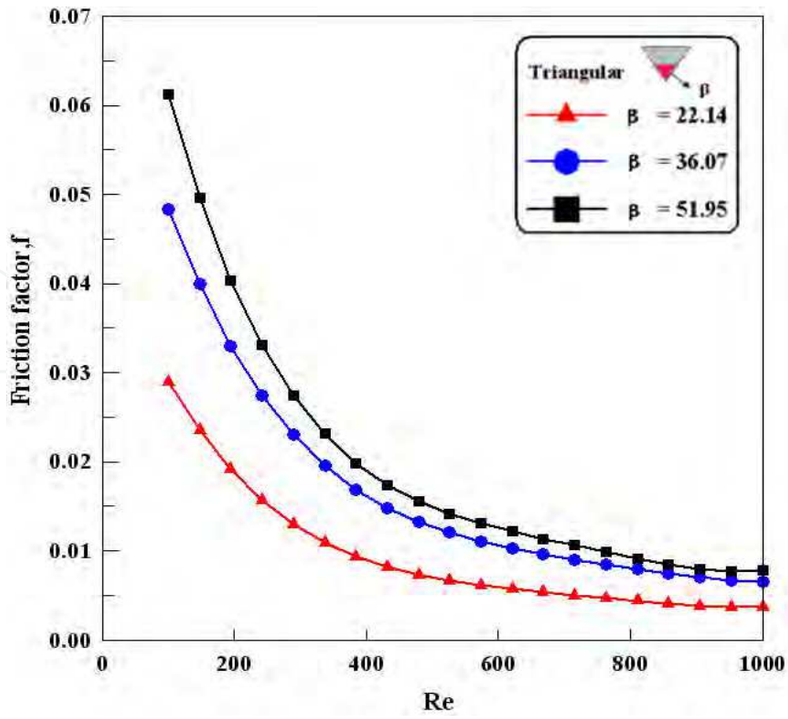

Fig. 3.7. Friction factor with different tip angles of triangular cross-section MCHS.

3.4 Thermal resistance

The performance of the MCHS is commonly presented by the thermal resistance (R_{th}) which is defined as:

$$R_{th} = \frac{T_{w,\max} - T_{in}}{Q_{in}} \tag{3.3}$$

Another important parameter in MCHS operation is the pressure drop across the MCHS which relates to the coolant pumping power required. The pumping power is used to drive the coolant in MCHS operation. It is the product of the pressure drop across the heat sink, ΔP and volume flow rate, Q:

$$\text{Pumping power} = Q\Delta P \tag{3.4}$$

where Q is defined as:
For rectangular cross-section MCHS,

$$Q = N\, W_{\text{ch}}\, H_{\text{ch}}\, u_{in} \tag{3.5}$$

where N is the number of microchannels, W_{ch} is the width of channel, H_{ch} is the height of channel, and u_{in} is the inlet velocity of water.
For trapezoidal cross-section MCHS,

$$Q = 0.5\, N\, (a + b)\, u_{in} \tag{3.6}$$

where N is the number of microchannels, k is the width of channel, h is the height of channel, and $u_{\text{in,nf}}$ is the inlet velocity of water.

For triangular cross-section MCHS,

$$Q = 0.5\, N\, k\, h\, u_{in} \tag{3.7}$$

where N is the number of microchannels, k is the width of channel, h is the height of channel, and u_{in} is the inlet velocity of water.

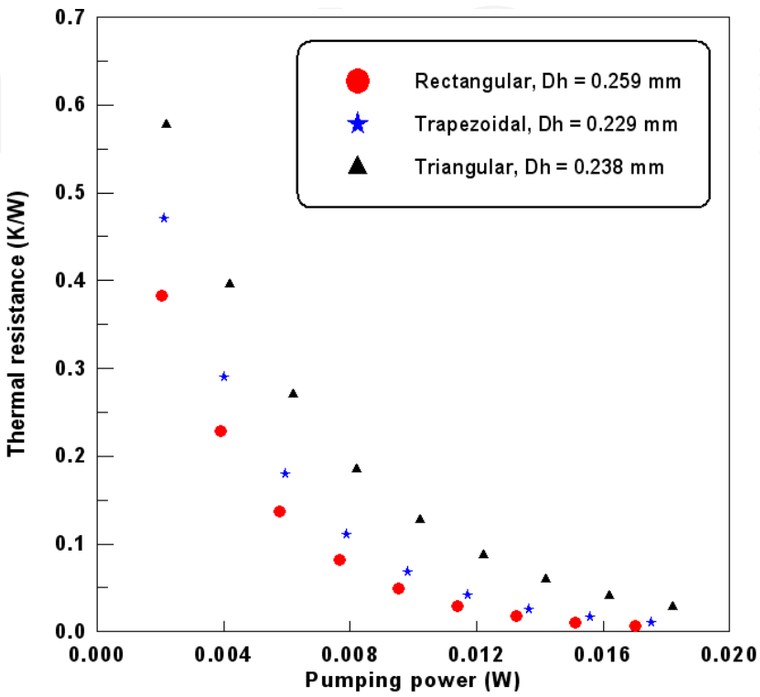

Fig. 3.8. Thermal resistance of MCHS with different cross-section shapes as function of pumping power.

The effect of using different cross sectional shapes of MCHS on thermal resistance, R_{th} versus pumping power is shown in Fig.3.8. The pumping power is determined from the calculated volume flow rate for rectangular, trapezoidal, and triangular cross-section shape using Eq.3.5-Eq.3.7, respectively, and computed pressure drop using Eq.3.4. It is evident from this figure that the R_{th} for rectangular cross-section MCHS is the lowest followed by trapezoidal and triangular cross-section MCHS. Thus, a MCHS with rectangular cross-section is capable for removing high heat flux due to its small difference between maximum wall temperature and inlet temperature at particular pumping power compared with that for MCHS with trapezoidal and triangular cross-sections.

4. Effect of nanoparticle volume fractions on MCHS performance

Nanofluids are produced from a suspension of nanoparticles with specified volume fraction in a conventional base fluid such as water, have been gaining interest recently due to its potential to greatly outperform traditional thermal transport liquids in MCHS [23]. However, the cooling effectiveness of using nanofluid as well as addressing other technical problems, such as agglomeration of the nanoparticles which yield to MCHS clogging due to the high particle volume fraction are vital to practical implementation of the nanofluid-

cooled MCHS. In the current study, the effect of using three different particle volume fractions on heat transfer and liquid flow characteristics in MCHS will be discussed. Since the cooling performance of MCHS with various cross sectional shapes is investigated in previous chapter, now a rectangular cross-section MCHS with specific dimensions as shown in Table 4.1 is considered. Results of interest such as temperature, heat transfer coefficient, friction factor, wall shear stress, and thermal resistance are reported in this section.
The forgoing thermophysical properties for the nanoparticle (alumina), base fluid (water), and the alumina-water nanofluid of three different volume fractions formulated are listed in Table 4.2. The density, thermal conductivity, and dynamic viscosity of the nanofluid appear significantly increased while the specific heat of nanofluid decreased with the increase of its particle volume fraction compared to pure water. The nanofluid of φ = 5% alumina, for instance, has a relative increase of 14.88%, 15.17%, and 12.46% in the density, thermal conductivity, and dynamic viscosity and has a relative decrease of 14.14% in specific heat, respectively, compared to pure water.

D_h (μm)	H_{ch} (μm)	W_{ch} (μm)	L_{ch} (μm)	S (μm)
339.15	43	280	10000	500

Table 4.1. Dimensions of the rectangular cross-section MCHS.

Properties	Nanoparticle	Base fluid	Nanofluid (alumina-water)		
	(alumina)	(water)	φ= 1%	φ= 2.5%	φ= 5%
ρ (kg/m^3)	3970	998.2	1027.92	1072.5	114 .79
Cp (J/kg.K)	765	4182	4050.03	3865.79	3590.55
k (W/m.K)	40	0.613	0.631	0.658	0.706
μ (Ns/m^2)		0.001003	0.001028	0.001066	0.001128

Table 4.2. Thermophysical properties of alumina nanoparticles, water, and nanofluid at 293K.

4.1 Thermophysical properties of nanofluid

In this study, aluminum oxide with different particle volume fractions is used as the working fluid. The thermophysical properties required for flow as listed in Table 4.2 are calculated using the following equations [24, 25, 26, 27]:

Density: $$\rho_{nf} = (1-\varphi)\,\rho_{bf} + \varphi\rho_p \tag{4.1}$$

Heat capacity: $$(\rho c_p)_{nf} = (1-\varphi)\,(\rho c_p)_{bf} + \varphi(\rho c_p)_p \tag{4.2}$$

Thermal conductivity: $$k_{nf} = \frac{k_p + 2k_{bf} + 2(k_p - k_{bf})\varphi}{k_p + 2k_{bf} - (k_p - k_{bf})\varphi} k_{bf} \quad (4.3)$$

Viscosity: $$\mu_{nf} = \mu_{bf}(1 + 2.5\varphi) \quad (4.4)$$

Where φ is particle volume fraction, the subscript "*nf*" refers to nanofluid, "*bf*" refers to base fluid, and "*p*" refers to particle.

4.2 Temperature profile

The dimensionless temperature distribution at each channel of MCHS at Re = 900 for various particle volume fractions and different heat fluxes is shown in Figs.4.1–4.3. The dimensionless temperature is calculated using Eq.3.1 (Section 3). The presence of nanoparticles has an effect of reducing the temperature as the particle volume fraction of nanofluids increasing due to its higher dynamic viscosity and lower heat capacity compared to pure water. However, these conditions only can be greatly achieved for the case of heat flux = 1000 W/m² compared to 100 W/m² and 500 W/m². For case 100 W/m² and 500 W/m², there is no significant differences between nanofluids and pure water, and the results are inconsistent for temperature distributions. Therefore, the presence of nanoparticles could enhance cooling of MCHS under the extreme heat flux conditions, the same trend was reported by Tsai and Chein [15] and Murshed et al. [28].

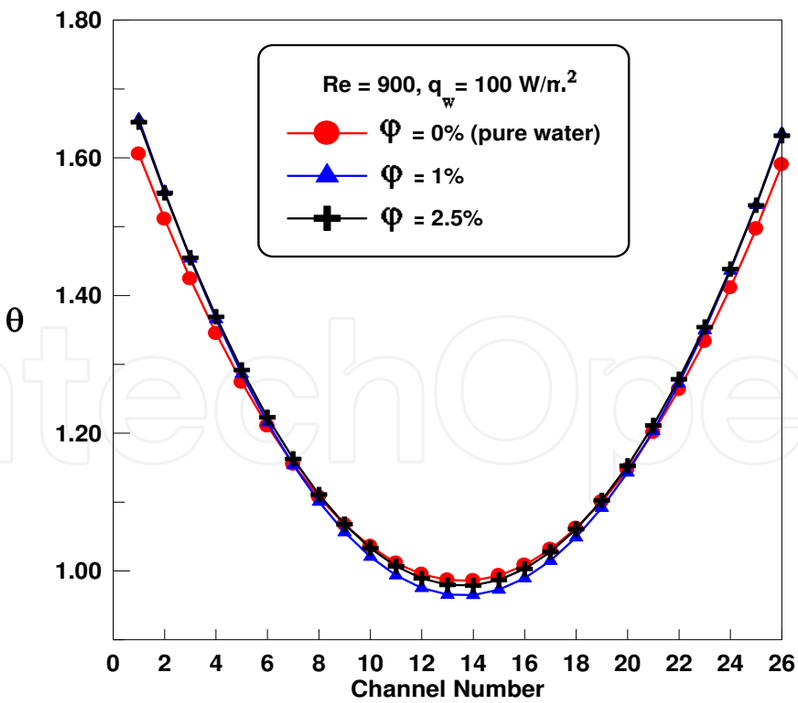

Fig. 4.1. Dimensionless temperature versus number of channels for 100 W/m².

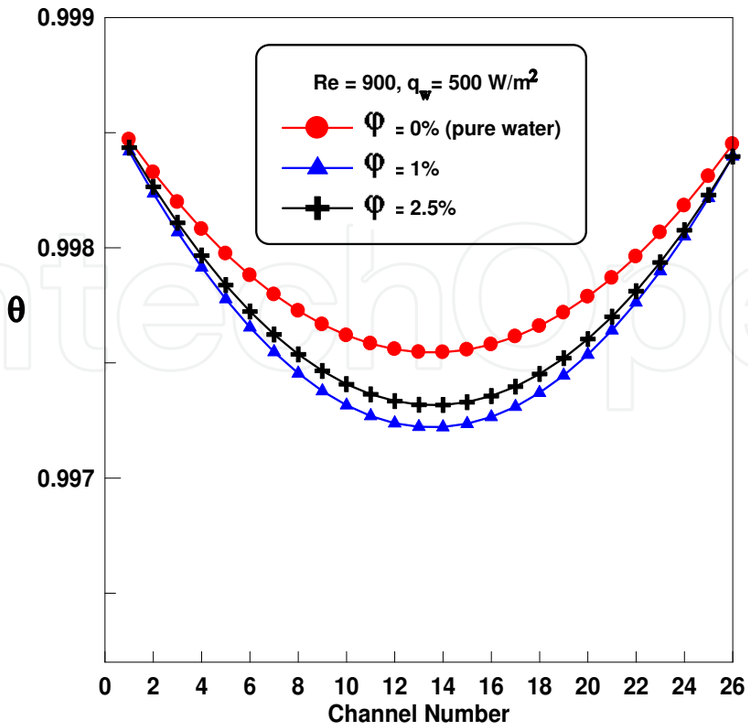

Fig. 4.2. Dimensionless temperature versus number of channels for 500 W/m².

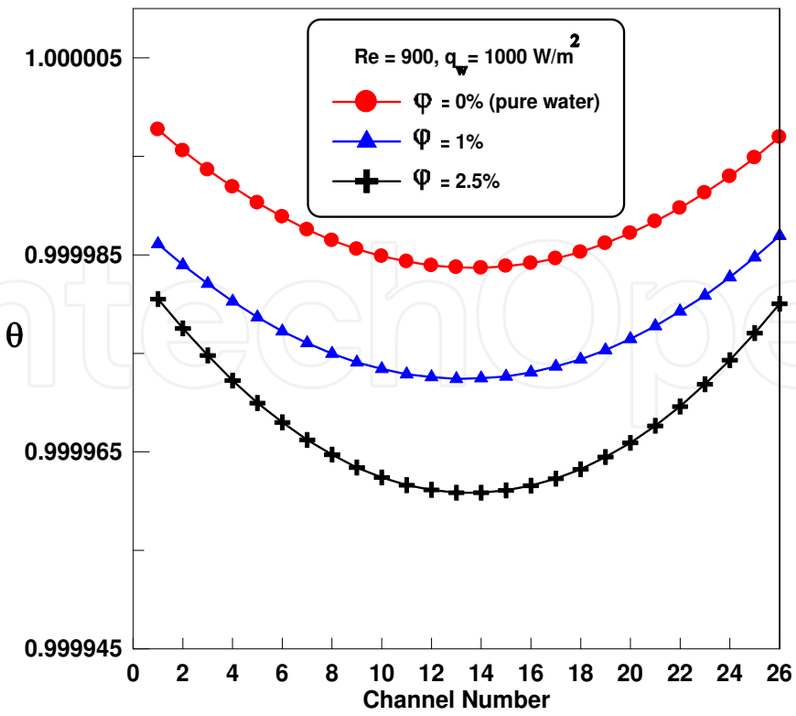

Fig. 4.3. Dimensionless temperature versus number of channels for 1000 W/m².

4.3 Heat transfer coefficient

The effect of increasing nanoparticle percentage volume fraction on the dimensionless heat transfer coefficient of the nanofluid in each channel of MCHS is shown in Fig.4.4. The dimensionless heat transfer coefficient is calculated using:

$$\hat{h} = \frac{h_{nf}}{h_{avg,water}} \tag{4.5}$$

Where h_{nf} is the nanofluids heat transfer coefficient value and $h_{avg,water}$ is the average heat transfer coefficient of pure water. It is inferred that the nanofluids can enhance the heat transfer of MCHS as its volume fraction increases from 0% to 2.5%. However, nanofluid with 5% volume fraction is not able to enhance the heat transfer or performing almost the same result as pure water. This may due to agglomeration of the nanoparticles. The validity of the present results is confirmed with Murshed et al. [28] results. From Fig.4.4, it is also observed that the middle channel (channel 14) has the highest averaged heat transfer coefficient value as expected. The averaged heat transfer coefficient value for other channels is seen to decrease depending on their distance from the wall. The present results as illustrated in Fig.5.6 show similar trend with the results obtained by Liu and Garimella [29] and Chein and Chen [19]. Since higher temperatures are observed due to the heat transfer from the high-temperature edge of the heat sink, the averaged heat transfer coefficient is lower in channels close to the edge of the heat sink.

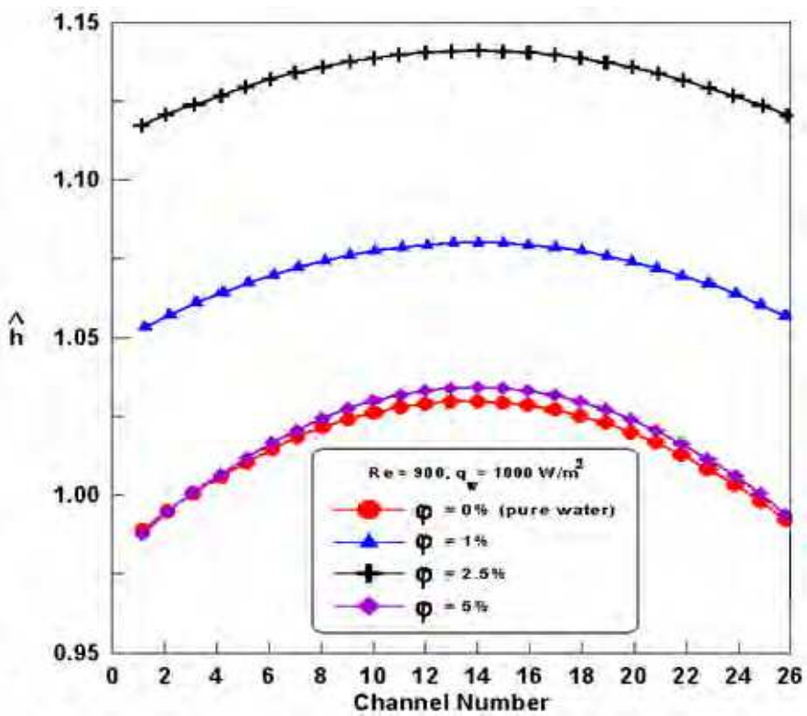

Fig. 4.4. Dimensionless averaged heat transfer coefficient versus number of channels for various particle volume fractions.

4.4 Friction factor

The variation of the friction factor for various particle volume fractions is shown in Figs.4.5 and 4.6 for Reynolds number ranged from100-500 and 500-1000, respectively. The friction factor is calculated using Darcy equation [20]:

$$f = \frac{2D_h \Delta p}{\rho_{nf} u_{in,nf}{}^2 L_c} \tag{4.6}$$

Where D_h is the hydraulic diameter, Δp is the pressure drop, ρ_{nf} is the density of nanofluid, $u_{in,nf}$ is the inlet velocity of nanofluid, and L_c is the length of channel.

The results show that the friction factor is similar for all particle volume fractions where the friction factor decreases with the increase of Reynolds number. Based on Figs.4.5 and 4.6, it can be stated that the increment of dynamic viscosity due to the presence of the nanoparticles in water, only appears to give a slight rise in friction factor especially for low Reynolds number range (Fig.4.5). For high Reynolds number range (Fig.4.6), the nanofluid flow yields significant effect on friction factor.

Fig.4.7 shows a comparison of the predicted friction factor from the present numerical simulation against previous experimental studies [12, 30]. A very good agreement was obtained for φ = 0% (pure) and φ = 1% alumina, which shows that the friction factor decreases with the increase of Reynolds number.

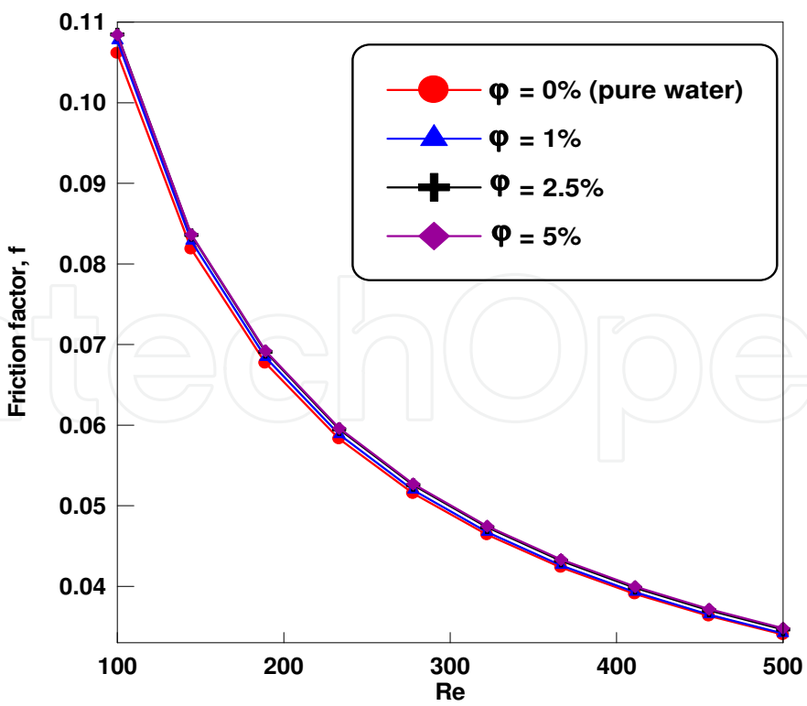

Fig. 4.5. Friction factor of MCHS for Reynolds number ranged from 100-500.

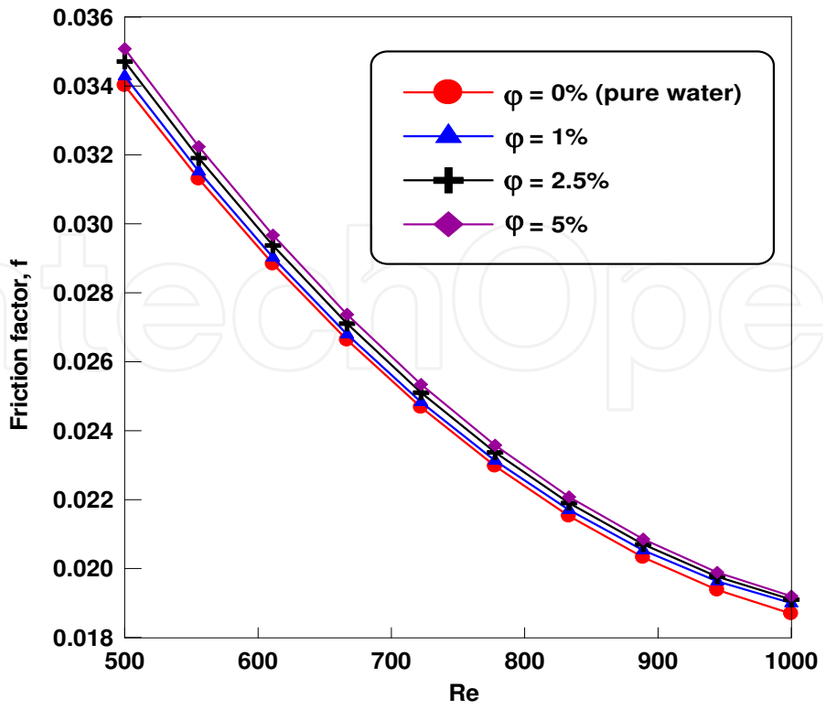

Fig. 4.6. Friction factor of MCHS for Reynolds number ranged from 500-1000.

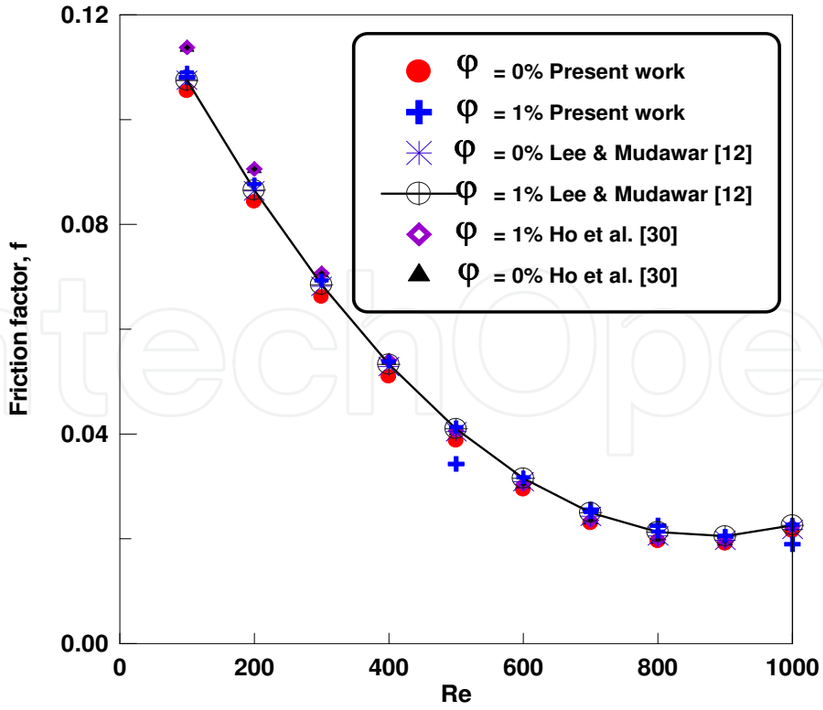

Fig. 4.7. A comparison of predicted friction factor with [12] and [30].

4.5 Wall shear stress

The effect of different volume fractions of nanoparticles on the local dimensionless wall shear stress is also investigated in the current study and the results are shown in Fig.4.8. The dimensionless wall shear stress is calculated using:

$$\hat{\tau} = \frac{\tau_{nf}}{\tau_{avg,water}} \tag{4.7}$$

Where τ_{nf} is the nanofluid wall shear stress and $\tau_{avg,\ water}$ is the average value of pure water wall shear stress.

As depicted in Fig.4.8, the wall shear stress increases with increasing Reynolds number for a specified percentage of volume fractions. It is clearly seen that for all cases investigated, the presence of nanoparticles substantially increases the wall shear-stress as compared with pure water. In general, for all cases examined, the least wall shear stress occurs at lower value of φ = 1 % while highest value occurs at φ = 5 %.

4.6 Thermal resistance

Since the maximum wall temperature ($T_{w,\ max}$) of nanofluid-cooled MCHS is lower than pure water-cooled MCHS, reduction of thermal resistance in nanofluid-cooled MCHS is then expected. If the presence of nanoparticles in coolant did not produce extra pressure drop which relates to the coolant pumping power required, it can then be considered as another benefit of using nanofluid as the coolant in MCHS operation. The volume flow rate, Q for rectangular shaped microchannel is defined as:

$$Q = N\, W_{\mathrm{ch}}\, H_{\mathrm{ch}}\, u_{in,\mathrm{nf}} \tag{4.8}$$

Where N is the number of microchannels, W_{ch} is the width of channel, H_{ch} is the height of channel, and $u_{in,\mathrm{nf}}$ is the inlet velocity of nanofluid.

The cooling performance of the MCHS using nanofluid is assessed by exploring the results for the thermal resistance, R_{th} as defined in Eq.3.3. The variation of thermal resistance versus pumping power is presented in Fig.4.9. The pumping power is determined from the calculated volume flow rate as defined in Eq.4.8 and computed pressure drop using Eq.3.4 (Section 3). As depicted in Fig.4.9, the nanofluid is shown to have significantly lower value of R_{th} as its particle volume fraction increases than pure water. For the current geometry under study, the maximum reduction in R_{th} that can
be achieved is about 57.6% for nanofluid with particle volume fraction of 5% at 0.0145 W. This great improvement in R_{th} is mainly due to the increase in thermal conductivity and decrease in temperature difference between inlet and maximum wall temperature as the particle volume fraction increases. The additional reduction in R_{th} is clearly due to the thermal dispersion. Since water has the highest R_{th} value, it is not preferable for removing high heat flux. The percent enhancement of MCHS's cooling performance is actually calculated by using:

$$\frac{R_{th,nf} - R_{th,water}}{R_{th,water}} x100\% \tag{4.9}$$

Where $R_{th,nf}$ corresponds to thermal resistance of particular nanofluid and $R_{th,water}$ corresponds to thermal resistance of pure water.

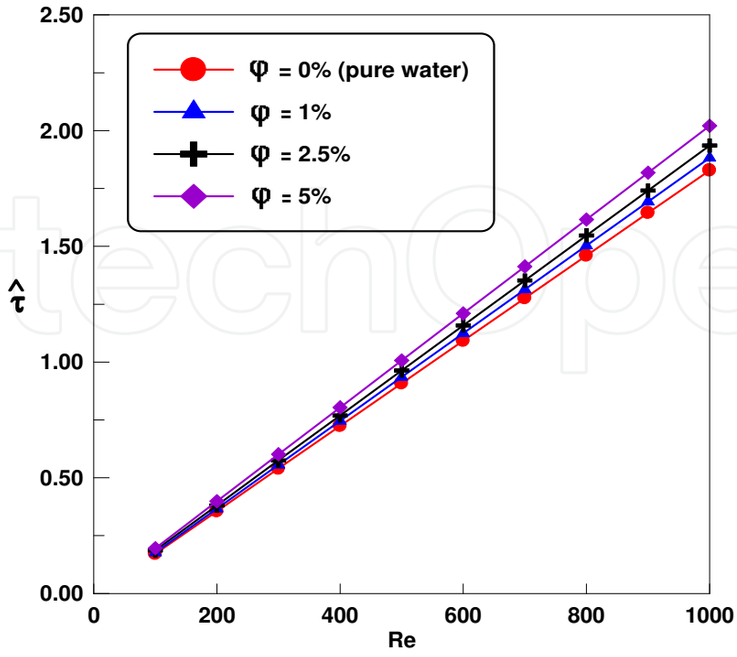

Fig. 4.8. Dimensionless wall shear stress versus Reynolds number for various particle volume fractions.

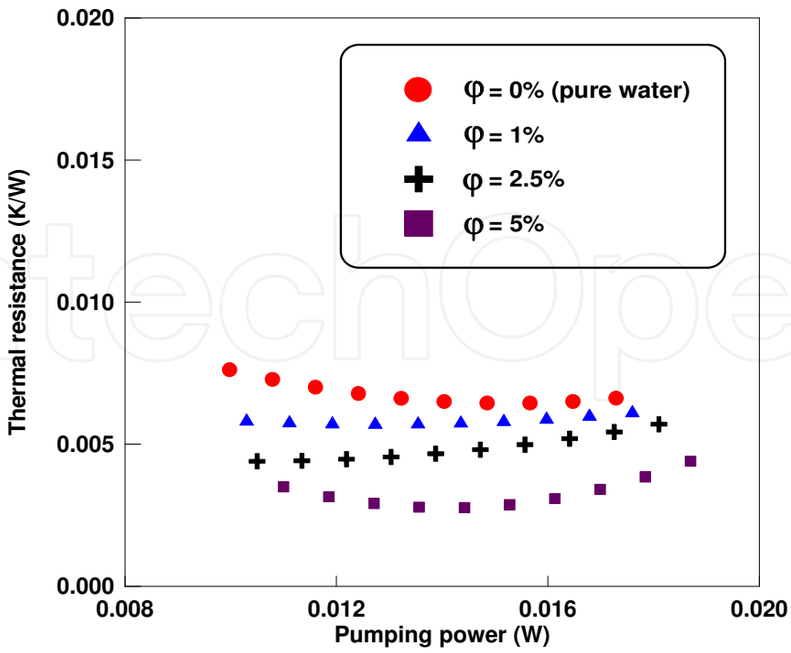

Fig. 4.9. Thermal resistance of MCHS as function of pumping power.

5. Effect of using different nanofluids on MCHS performance

Based on the results that obtained in Section 4 which focused on the effect of using different particle volume fractions of Al_2O_3-H_2O on heat transfer and liquid flow characteristics in MCHS, it is known that nanofluids have the capability to enhance the heat transfer performance of MCHS with smaller pressure drop penalty. However, due to production of various nanofluids in market, further investigations on using different types of nanofluids in MCHS are necessary because the heat transfer enhancement of MCHS is strongly depend on thermophysical properties of dispersed nanoparticles in base fluid [31]. Thus, in this chapter, the effect of using six types of nanofluids on heat transfer and liquid flow characteristics in triangular cross-section MCHS with specified dimensions is comprehensively investigated.

The specific dimensions of the triangular MCHS used in this section are given in Table 5.1. A constant particle volume fraction value of 2% is considered for all types of nanofluids studied in this chapter. The thermophysical properties for all types of nanoparticles, base fluid (water), and the nanofluids with particle volume fraction of 2% are listed in Table 5.2. For all types of nanofluids studied, the density, thermal conductivity, and dynamic viscosity appear significantly higher while the specific heat of nanofluids is lower than pure water. For instance, diamond-H_2O nanofluid has a relative increase of 5.03%, 6.11%, and 5% in the density, thermal conductivity, and dynamic viscosity and has a relative decrease of 5.90% in specific heat, respectively, compared with pure water.

In this section, different types of nanofluids which are Al_2O_3-H_2O, Ag-H_2O, CuO-H_2O, diamond-H_2O, SiO_2-H_2O, and TiO_2-H_2O are used as working fluids. The thermophysical properties as listed in Table 5.2 including density, heat capacity, thermal conductivity, and viscosity for all types of nanofluids which are involved in the governing equations are calculated using Eqs.4.1-4.4 (Section 4), respectively.

5.1 Heat transfer coefficient

The thermal performance of using different types of nanofluids in MCHS is examined by presenting the results of the dimensionless heat transfer coefficient along the length of channel number 1 in Fig.5.1. It is observed that all types of nanofluids-cooled MCHS could be able to enhance the heat transfer compared with pure water-cooled MCHS. The water-base nanofluid containing diamond has the highest heat transfer coefficient value followed by SiO_2, CuO, TiO_2, Ag and Al_2O_3. However, there is no significant difference that can be detected between TiO_2 and CuO due to their small difference in thermal diffusivity. However, there is a very small increment in CuO-H_2O-cooled MCHS especially at the outlet of the channel compared with that for TiO_2-H_2O-cooled MCHS.

Dh (μm)	k (μm)	h (μm)	l (μm)	Lch (μm)	S (μm)	β
230	280	430	452	10000	500	36.07o

Table 5.1. Dimensions of the triangular cross-section MCHS.

Properties	Nanoparticle (diamond)	Base fluid (water)	Nanofluid (diamond-H_2O) $\varphi = 2\%$
ρ (kg/m^3)	3510	998.2	1048.436
Cp (J/kg.K)	497.26	4182	3935.28
κ (W/m.K)	1000	0.613	0.65046
μ (Ns/m^2)		0.001003	0.00105315
Properties	Nanoparticle (silicon dioxide)	Base fluid (water)	Nanofluid (SiO_2-H_2O) $\varphi = 2\%$
ρ (kg/m^3)	2200	998.2	1022.236
Cp (J/kg.K)	703	4182	4032.25
κ (W/m.K)	1.2	0.613	0.62194
μ (Ns/m^2)		0.001003	0.00105315
Properties	Nanoparticle (copper oxide)	Base fluid (water)	Nanofluid (CuO-H_2O) $\varphi = 2\%$
ρ (kg/m^3)	6500	998.2	1108.236
Cp (J/kg.K)	535.6	4182	3754.26
κ (W/m.K)	20	0.613	0.64722
μ (Ns/m^2)		0.001003	0.00105315
Properties	Nanoparticle (titanium dioxide)	Base fluid (water)	Nanofluid (TiO_2-H_2O) $\varphi = 2\%$
ρ (kg/m^3)	4250	998.2	1063.236
Cp (J/kg.K)	686.2	4182	3902.53
κ (W/m.K))	8.9538	0.613	0.64364
μ (Ns/m^2)		0.001003	0.00105315
Properties	Nanoparticle (silver)	Base fluid (water)	Nanofluid (Ag-H_2O) $\varphi = 2\%$
ρ (kg/m^3)	10500	998.2	1188.236
Cp (J/kg.K)	235	4182	3484.44
κ (W/m.K)	429	0.613	0.65037
μ (Ns/m^2)		0.001003	0.00105315
Properties	Nanoparticle (aluminum oxide)	Base fluid (water)	Nanofluid (Al_2O_3-H_2O) $\varphi = 2\%$
ρ (kg/m^3)	3970	998.2	1057.636
Cp (J/kg.K)	765	4182	3925.47526
κ (W/m.K)	40	0.613	0.64882
μ (Ns/m^2)		0.001003	0.00105315

Table 5.2. Thermophysical properties of nanoparticles, water and nanofluids at 293K.

Since the velocity at the entrance of the channel was kept constant at Re = 600, it can be noticed that the heat transfer coefficient decreases linearly along the length of channel because of the development of thermal boundary layer for all cases. The highest value of heat transfer coefficient occurs near the entrance. The present results show a similar trend with the results obtained by Lee and Mudawar [12]. It is also depicted from Fig.5.1 that the difference in dimensionless heat transfer coefficient between various nanofluids is too small but it follows trend and not too far from reported values. From the results obtained, lowest
thermal resistance is expected with diamond-H_2O nanofluid cooled MCHS due to its lowest temperature distribution. Therefore, the presence of diamond nanoparticle in water could greatly enhance the cooling of MCHS compared with other types of nanofluids. This is due to the highest thermal transport capacity of diamond in nature and diamond particles are often used as filler in mixtures for upgrading the performance of a matrix (composition of mixtures) as reported by Xie et al. [32]. Thus, it is reasonable to expect that the addition of diamond nanoparticles in water would lead to heat transfer enhancement.

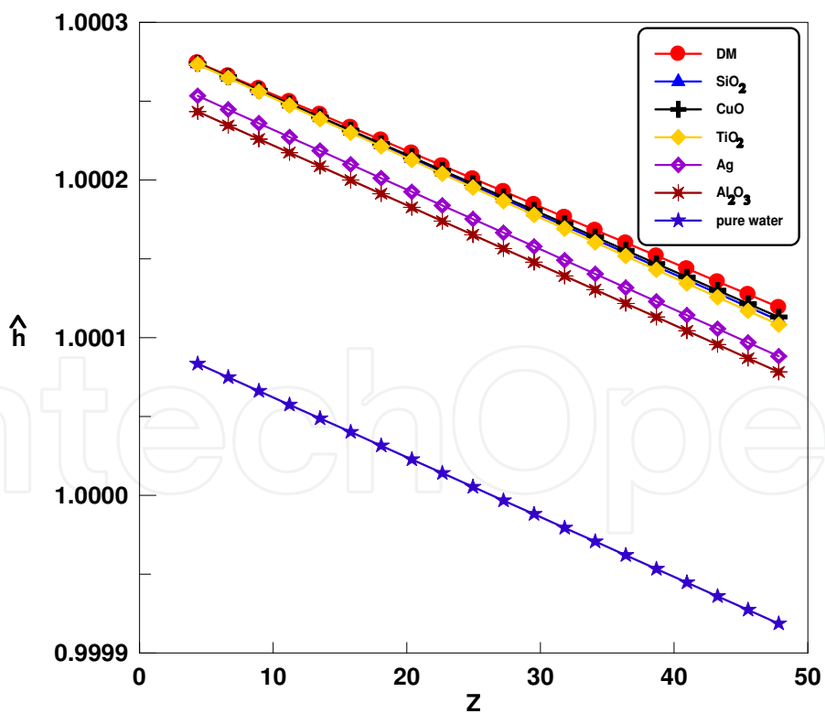

Fig. 5.1. Dimensionless heat transfer coefficient along the length of channel No.1.

5.2 Pressure drop

The dimensionless pressure distribution of the MCHS for various nanofluids and pure water along the length of channel number 1 is shown in Fig.5.2. The dimensionless pressure distribution is calculated using:

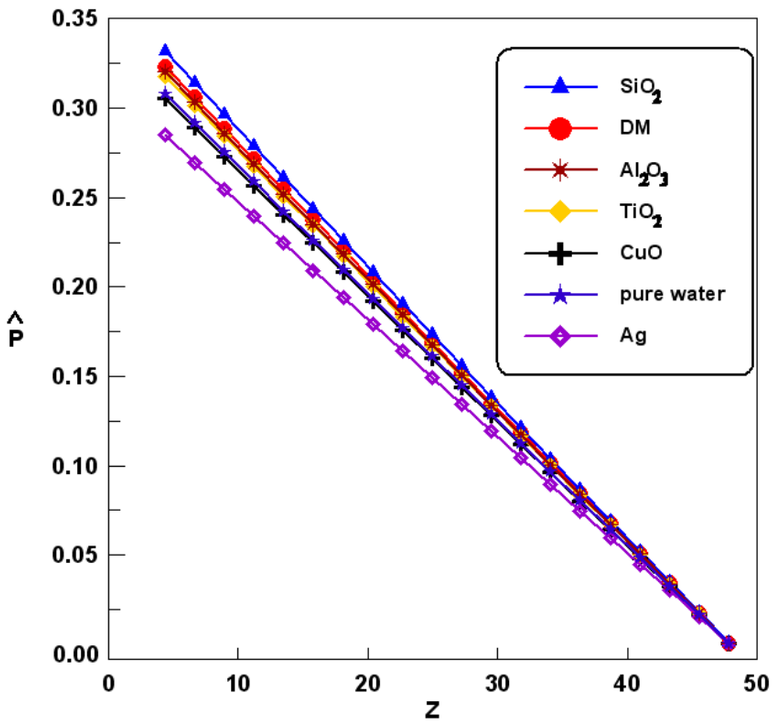

Fig. 5.2. Dimensionless pressure drop variation along the length of channel No.1.

$$\hat{P} = \frac{\Delta P}{\rho u_{in}^2} \tag{5.1}$$

where ΔP is the pressure drop of particular microchannel configuration, ρ is the water density, and u_{in} is the inlet water velocity.

It can obviously be seen that the high pressure region occurs at the entrance and the low pressure region occurs at the outlet of the heat sink. This is due to the needs of high pressure to push the fluid flow along the direction of the microchannels out from the outlet plenum of heat sink. Thus, the pressure decreases linearly along the length of channel for all types of nanofluids studied including pure water. Because of that, there is no apparent difference observed between pure water and nanofluids flows particularly at the outlet region of MCHS. However, compared with pure water cooled case, slightly larger pressure drops for nanofluid-cooled MCHS were found except for Ag-H_2O nanofluid which has the lowest value of pressure drop among nanofluids types. The water-base nanofluids containing SiO_2 has the highest value of pressure drop and followed by diamond-H_2O respectively. The pressure drop in water-base nanofluids-cooled MCHS containing Al_2O_3 and TiO_2 are slightly lower than diamond-H_2O-cooled MCHS.

Since the viscosity of nanofluids is larger than pure water as indicated in Table 5.2, larger pressure drop is expected in nanofluid-cooled MCHS. Another reason that contributes to increase the pressure drop is the deposition of nanoparticle in water is increasing the wall

roughness [28]. However, Ag-H_2O-cooled MCHS still has lower value of pressure drop than pure water-cooled MCHS and there is no extra pressure drop in CuO-H_2O-cooled MCHS as compared with pure water-cooled MCHS. The reason for this result is Ag-H_2O has the lowest Prandtl number (Pr = 5.6 and followed by CuO-H_2O (Pr = 6.1). The small difference in pressure drop between other types of nanofluids which can be seen in Fig.5.2 is due to small differences in their Prandtl numbers and SiO_2-H_2O yields the highest pressure drop across the MCHS due to its highest Prandtl number (Pr = 6.8). Therefore, the pressure drop penalty is not only affected by the viscosity of nanofluids but also the Prandtl number of nanofluids which need to be considered in nanofluids selection as a coolant for MCHS. Apart from that, slight increment in pressure drop particularly for Ag-H_2O and CuO-H_2O-cooled MCHS which can be considered as one of the benefits of using nanofluid in MCHS operations in order to achieve overall heat transfer enhancement with small pressure drop penalty.

5.3 Thermal resistance

The pumping power which is the product of the pressure drop across the heat sink, ΔP and volume flow rate, Q, is calculated using Eq.3.4. The volume flow rate, Q for triangular shaped microchannel is defined as:

$$Q = 0.5\, N\, k\, h\, u_{\text{in,nf}} \tag{5.1}$$

Where N is the number of microchannels, k is the width of channel, h is the height of channel, and $u_{\text{in,nf}}$ is the inlet velocity of nanofluid.

The thermal resistance for all types of nanofluids as function of pumping power is shown in Fig.5.3. It is observed that all types of nanofluids reduce the thermal resistance of MCHS

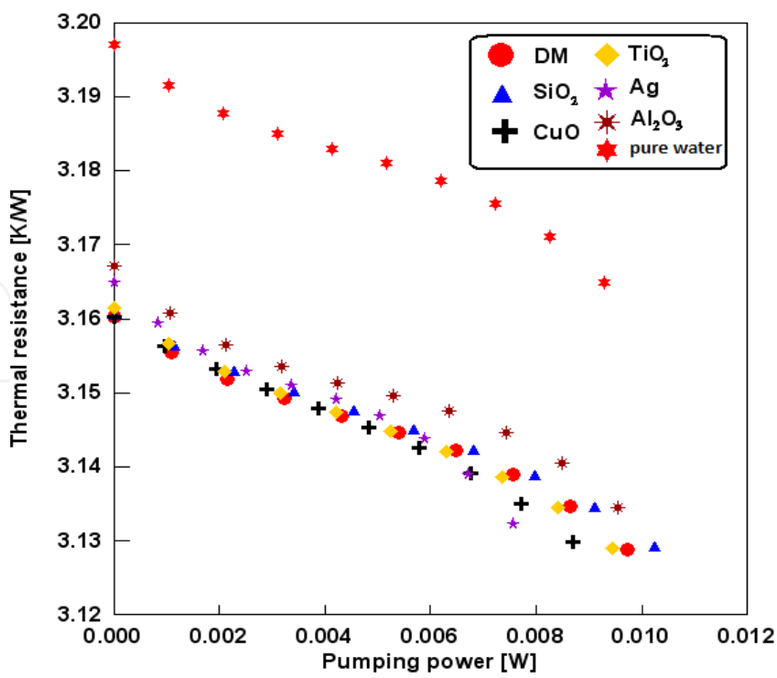

Fig. 5.3. Thermal resistance of MCHS as function of pumping power.

than pure water. The maximum reduction in R_{th} is achieved in diamond-H_2O MCHS is 3.1292 K/W when pumping power is 0.0097207 W. The results indicate that the cooling performance of a MCHS at pumping power = 0.005 W is enhanced by about 2 % for water-base nanofluids containing diamond, SiO_2, CuO, and TiO_2, 1.13% for water-base nanofluids containing Al_2O_3, and 1.04% for water-base nanofluids containing Ag respectively, compared with that of the MCHS with pure water. The percent enhancement of MCHS cooling performance is also calculated using Eq.4.9. The great improvement in R_{th} is mainly due to the increase in thermal conductivity and decrease in temperature difference between inlet and maximum wall temperature. The additional reduction in R_{th} is also due to the thermal dispersion of particle volume fractions.

6. Effect of using different base fluids on MCHS performance

Since base fluid for all types of nanofluids studied in Section 5 was water, it is important and necessary to know the heat transfer and liquid flow characteristics in MCHS using other types of conventional base fluids such as ethylene glycol (EG), glycerin, and oil. By using other types of conventional base fluids instead of using water, the MCHS cooling performance could be enhanced or may not. Thus, considering nanofluid flow in a microchannel, the effect of using different types of base fluids including water, EG, engine oil, and glycerin on heat transfer and liquid flow characteristics in trapezoidal shaped MCHS which was selected for this chapter with specified dimensions is extensively discussed in this chapter. The specified dimensions are given in Table 6.1.

Since the best uniformities in heat transfer coefficient and temperature can be achieved in MCHS using diamond nanoparticle as obtained in Section 5, the diamond nanoparticle is selected and considered for all types of base fluids studied in this chapter. The thermophysical properties for diamond nanoparticle, for all types of base fluids, and the nanofluids with particle volume fraction of 2% formulated are listed in Table 6.2. For all types of nanofluids, the density, thermal conductivity, and dynamic viscosity appear significantly higher while the specific heat of nanofluids is lower than the base fluids. For instance, the EG-diamond nanofluid has a relative increase of 4.28%, 6.12%, and 5% in the density, thermal conductivity, and dynamic viscosity and has a relative decrease of 4.77% in specific heat, respectively, compared with EG base fluid.

The thermophysical properties as listed in Table 6.2 including density, heat capacity, thermal conductivity, and viscosity for all types of base fluids for nanoparticles are calculated using Eqs.4.1-4.4 (Section 4), respectively.

Dh (μm)	a (μm)	b (μm)	c (μm)	Lch (μm)	h (μm)
318	280	225	431	10000	430

Table 6.1. Dimensions of the trapezoidal cross-section MCHS.

Properties	Nanoparticle (Diamond)	Base fluid (Water)	Nanofluid (H_2O-Diamond) $\varphi = 2\%$
ρ (kg/m^3)	3510	998.2	1048.436
Cp (J/kg.K)	497.26	4182	3935.28
κ (W/m.K)	1000	0.613	0.65046
μ (Ns/m^2)		0.001003	0.00105315
Properties	Nanoparticle (Diamond)	Base fluid (Ethylene Glycol)	Nanofluid (EG-Diamond) $\varphi = 2\%$
ρ (kg/m^3)	3510	1117.48	1165.33
Cp (J/kg.K)	497.26	2382.1	2268.56
κ (W/m.K)	1000	0.2492	0.26445
μ (Ns/m^2)		0.022	0.0231
Properties	Nanoparticle (Diamond)	Base fluid (Oil)	Nanofluid (Oil-Diamond) $\varphi = 2\%$
ρ (kg/m^3)	3510	888.23	940.665
Cp (J/kg.K)	497.26	1880.3	1777.09
κ (W/m.K)	1000	0.145	0.15387
μ (Ns/m^2)		0.8451	0.88736
Properties	Nanoparticle (Diamond)	Base fluid (Glycerin)	Nanofluid (Glycerin-Diamond) $\varphi = 2\%$
ρ (kg/m^3)	3510	1264.03	1308.95
Cp (J/kg.K)	497.26	2385	2283.76
κ (W/m.K))	1000	0.286	0.30349
μ (Ns/m^2)		1.5347	1.61144

Table 6.2. Thermophysical properties of diamond nanoparticels, base fluids and nanofluids at 293K.

6.1 Temperature profile

The effect of different types of base fluids on dimensionless temperature variation is presented in Fig.6.1. It can clearly be seen that the temperature of pure water is always highest among all types of base fluids. By comparing dimensionless temperature distributions between different types of base fluids, glycerin-diamond has the lowest value of temperature while water-diamond has the highest value of temperature and followed by EG-diamond and oil-diamond. Based on results shown in Fig.6.1, it can be stated that the lowest thermal resistance is expected in the glycerin-diamond fluid cooled MCHS due to its lowest temperature distribution. Therefore, the presence of diamond nanoparticle in glycerin could greatly enhance the cooling of MCHS compared with other types of base fluids studied. This is because of glycerin has the highest dynamic viscosity in nature compared to other base fluids and diamond particle mixed properly in glycerin which contribute to increase the thermal transport capacity of the mixture.

6.2 Heat transfer coefficient

The thermal performance of using different types of base fluids in MCHS is examined by plotting results of the dimensionless heat transfer coefficient along the length of channel number 20 as shown in Fig.6.2. Koo and Kleinstreuer [10] reported that higher Prandtl number base fluids-cooled MCHS could be able to enhance the heat transfer performance of MCHS as compared with water base-cooled MCHS. This was proven by the present results where the glycerin base-cooled MCHS has the highest $\hat{h}$ value due to the highest Prandtl number value followed by oil, and EG.

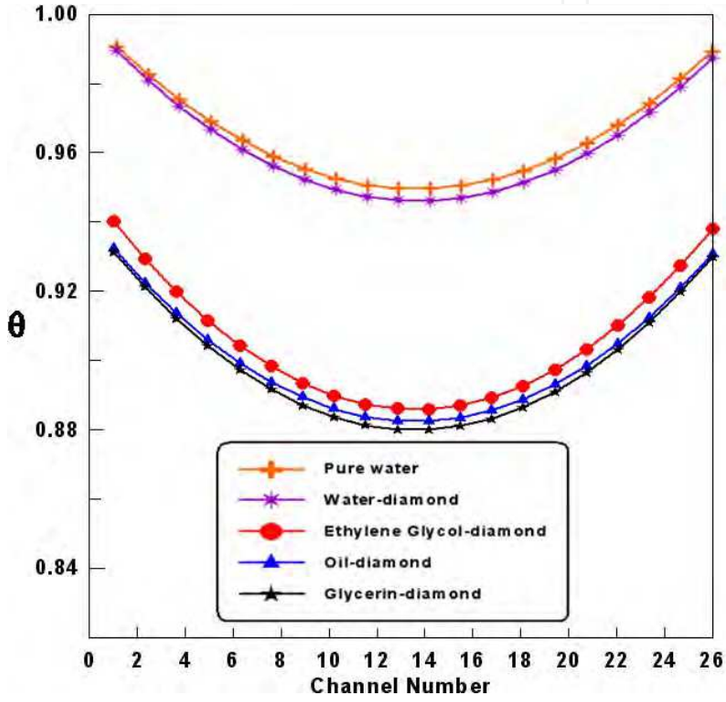

Fig. 6.1. Dimensionless temperature profile versus number of channels for pure water and various base fluids.

Fig.6.3 shows the dimensionless heat transfer coefficient in each channel of the heat sinks for various base fluids-cooled MCHS. The $\hat{h}$ for high Prandtl number base fluids is always higher than that for water base fluid. This is due to the fact that high Prandtl number base fluids are experiencing stronger thermal flow development effects as reported by Koo and Kleinstreuer [10]. However, there is no significant differences in $\hat{h}$ for EG, oil, and glycerine but when the plot is zoomed in, there are slight differences in $\hat{h}$ where glycerin base-cooled MCHS has the highest $\hat{h}$ value, oil is in between, and EG is the least. For each type of the heat sinks, the middle channel (channel number 14) has the highest $\hat{h}$ value as expected. The averaged heat transfer coefficient value for other channels is seen to decrease depending on their distances from the wall. The averaged heat transfer coefficient distribution for all types of MCHS is almost symmetrical with respect to the centreline of the heat sink.

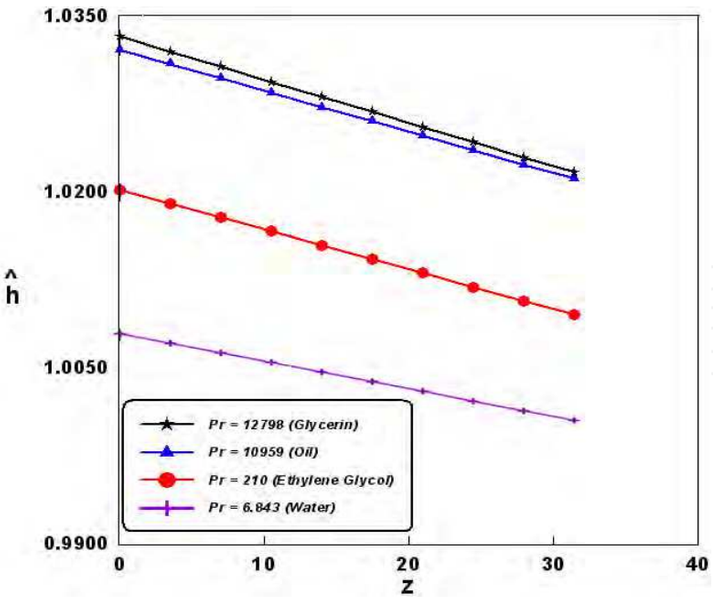

Fig. 6.2. Dimensionless heat transfer coefficient along the length of channel No.20 for various base fluids.

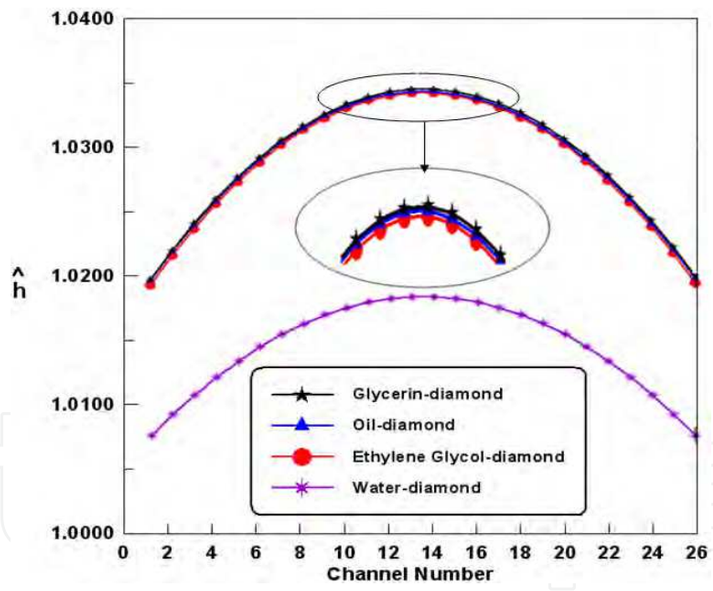

Fig. 6.3. Dimensionless averaged heat transfer coefficient versus number of channels for various base fluids.

Fig.6.4 shows the dimensionless heat transfer coefficient in each channel of various substrate materials for EG-base fluid. The highest $\hat{h}$ is achieved in copper made microchannels, which has the lowest thermal diffusivity followed by aluminium, steel, and titanium. The increase in $\hat{h}$ could be attributed to the decreased conduction resistance along the microchannel wall due to much lower thermal diffusivity in copper made microchannels. The averaged heat transfer coefficient of oil and glycerine base-cooled MCHS shows a similar trend as for EG base-cooled MCHS. However, the condition becomes different for low Prandtl number base

fluid (water) where the highest $\hat{h}$ is present in steel made microchannels as depicted in Fig.6.5. This proves that the thermal diffusivity of substrate material on the heat transfer in micro domains has significant effect for low and high Prandtl number base fluids. Thus, based on the results presented in Fig.6.5, it can be stated that the heat transfer performance of a low Prandtl number base fluid such as water can be greatly enhanced by using it as a coolant in MCHS of a high thermal diffusivity made substrate material such as steel.

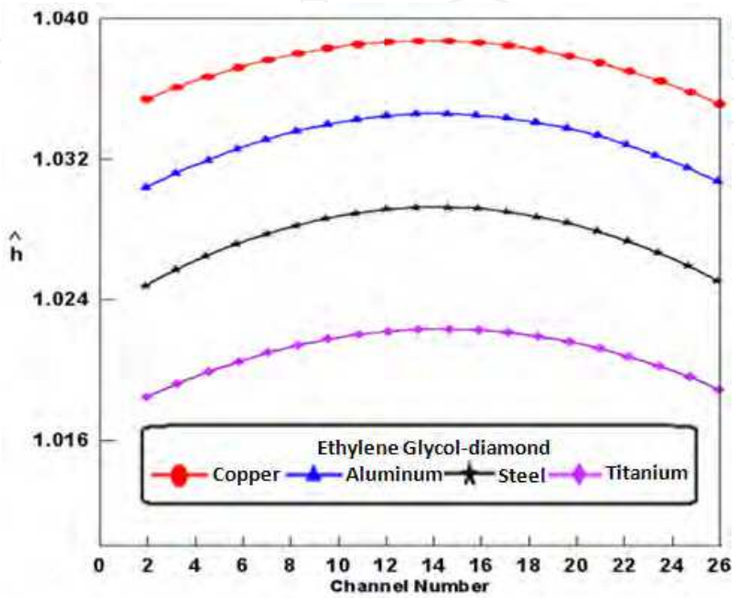

Fig. 6.4. Dimensionless averaged heat transfer coefficient versus number of channels for ethylene glycol-base nanofluid with different substrate materials.

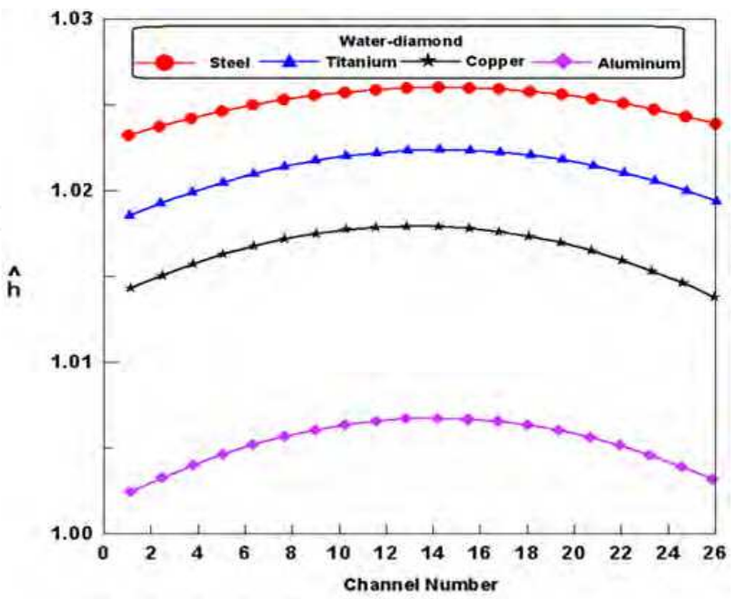

Fig. 6.5. Dimensionless averaged heat transfer coefficient versus number of channels for water-base nanofluid with different substrate materials.

6.3 Pressure drop

The variation of dimensionless pressure of the MCHS for various base fluids along the length of channel number 20 is presented in Fig.6.6. It can obviously be seen that the high pressure region occurs at the entrance and the low pressure region occurs at the outlet of MCHS. This is due to the needs of high pressure to push the fluid flow along the direction of the microchannels out from the outlet plenum of heat sink. Thus, the pressure decreases linearly along the length of channel for all types of base fluids studied.

The higher $\hat{P}$ for nanofluid-cooled MCHS is found in high Prandtl number base fluids due to the highest dynamic viscosity as stated in Table 6.2 as reported by Koo and Kleinstreuer [10]. The water base-cooled MCHS has the lowest value of pressure drop due to its lowest dynamic viscosity among other base fluids. There is no apparent difference in $\hat{P}$ between EG, oil and glycerin as can be seen in Fig.6.6 although glycerin has the highest value of $\hat{P}$ followed by oil and EG, respectively. Since the dynamic viscosity of EG, oil and glycerin base fluids is larger than water, larger pressure drop is expected in the high Prandtl number base fluids than the low Prandtl number base fluids. Thus, selection of high Prandtl number base fluids as coolant in MCHS should be considered in balancing heat transfer enhancement and pressure drop penalty.

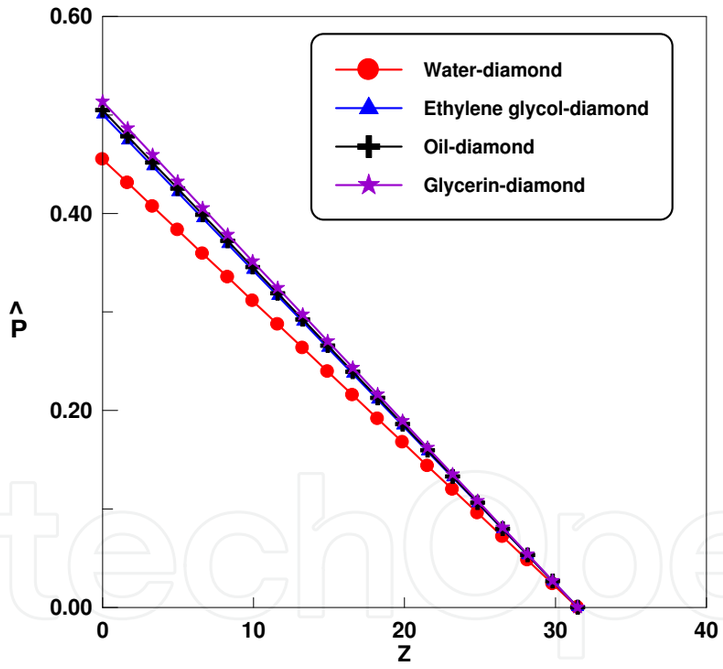

Fig. 6.6. Dimensionless pressure drop variation along the length of channel No.20.

7. Conclusions

The cooling efficiency of MCHS is numerically investigated using the FVM in this study. A three-dimensional model, fully developed laminar flow and heat transfer governing equations are solved using the finite volume method. Based on these effects, several conclusions can be drawn from all the simulation results.

For the effects of MCHS geometrical parameters:

- The width to height ratio (W_c/H_c) has a significant effect on the Poiseuille number for the rectangular cross-section microchannels. Poiseuille number increases linearly with the increase of W_c/H_c.
- For the trapezoidal cross-section MCHS, the height-to-top width ratio (H/a), the bottom-to-top width ratio (b/a), and length-to-hydraulic diameter ratio (L/D_h) are the important design parameters for trapezoidal microchannels. Poiseuille number increases linearly when H/a and L/D_h decreases while b/a increases.
- The tip angle (β) has a remarkable effect on the Poiseuille number for the triangular cross-section MCHS. Poiseuille number increases linearly with the increase of β.
- In order to achieve overall heat transfer enhancement in MCHS, it is envision that rectangular cross-section MCHS with a small hydraulic diameter was of greater benefit to the heat transfer coefficient with a lower penalty in pressure drop and friction factor compared with trapezoidal and triangular cross section MCHS.

For nanofluids in MCHS:

- The cooling performance of MCHS improved well when the particle volume fraction increases. However, the heat transfer becomes poor in larger amount of particle volume fraction of nanofluid flow as the heat transfer could not be enhanced compared with pure water.
- The presence of nanoparticles substantially increases the friction factor and wall shear stress. Both are rises with the increase of particle volume fractions.
- The nanofluid-cooled MCHS has lower thermal resistance than pure water-cooled MCHS. The thermal resistance decreases as the particle volume fraction increases.
- Diamond nanoparticles dispersed in water is preferable since diamond-H_2O-cooled MCHS has highest heat transfer coefficient value among the others.
- Ag nanoparticles dispersed in water is recommended as it has lowest pressure drop and wall shear stress among the other nanofluids studied.
- In order to achieve overall heat transfer enhancement, a base fluid of high Prandtl number (210-12800) such as glycerin, oil, and ethylene should be used to maximize the merits of adding nanoparticles for fluid flow in MCHS.
- Different types of base fluids do not have a significant influence on the friction factor.
- The heat transfer for low Prandtl number fluid flow such as water is greatly enhanced in high thermal diffusivity made material such as steel compared with low thermal diffusivity materials. These findings suggest that for low Prandtl number base fluids, the substrate material of high thermal diffusivity is desirable and vice versa in order to achieve a better heat transfer in MCHS.

8. Nomenclature

A	channel flow area, m^2
a	channel top width for trapezoidal cross-section MCHS, μm
Ag	silver
Al	aluminum
Al_2O_3	aluminum oxide
b	channel bottom width for trapezoidal cross-section MCHS, μm
c	channel hypotenuse for trapezoidal cross-section MCHS, μm
c_p	specific heat, J/kg.K

Cu	copper
CuO	copper oxide
D_h	hydraulic diameter, μm
DM	diamond
EG	Ethylene Glycol
f	friction factor
fRe	Poiseuille number
FV	Finite Volume
FVM	Finite Volume Method
h	heat transfer coefficient, $W/m^2.K$
h	channel height for trapezoidal and triangular cross-section MCHS, μm
$\hat{h}$	dimensionless heat transfer coefficient
H_{ch}	channel height for rectangular cross-section MCHS, μm
H_2O	water
k	channel width for triangular cross-section MCHS, μm
κ	thermal conductivity, W/m.K
κ_s	solid thermal conductivity, W/m.K
l	channel hypotenuse for triangular cross-section MCHS, μm
L_{ch}	channel length, μm
MCHS	Microchannel Heat Sink
n	direction normal to the wall
n	direction normal to the surface element
Nu	Nusselt number
P	channel wet perimeter, μm
$\hat{P}$	dimensionless pressure
P_{in}	inlet pressure, Pa
P_{out}	outlet pressure, Pa
Pr	Prandtl number
PW	pure water
Pow	pumping power, W
Q	volume flow rate, m^3/s
q_w	heat flux at microchannel heat sink top plate, W/m^2
Re	Reynolds number
R_{th}	thermal resistance, K/W
S	distance between two microchannels, μm
SiO_2	silicon dioxide
t	substrate thickness, μm
T	fluid phase temperature, K
Ti	titanium
TiO_2	titanium dioxide
T_{in}	fluid inlet temperature, K
T_s	microchannel heat sink solid temperature, K
u	fluid velocity, m/s
u_{in}	inlet fluid velocity, m/s
U	dimensionless velocity in x-coordinate
V	dimensionless velocity in y-coordinate

W	dimensionless velocity in z-coordinate
W_{ch}	channel width for rectangular cross-section MCHS, μm
X, Y, Z	dimensionless cartesian coordinates

Greek Symbols

a	thermal diffusivity, m^2/s
β	tip angle for triangular cross-section MCHS
μ	viscosity, kg/m.s
ρ	density, kg/m^3
τ	wall shear stress
$\hat{\tau}$	dimensionless wall shear stress
φ	particle volume fraction, %
θ	dimensionless temperature

Subscripts

avg	average
bf	base fluid
ch	channel
f	pure fluid
nf	nanofluid
h	hydraulic
i	inlet
o	outlet
s	solid
th	thermal
w	wall

9. Acknowledgements

The authors would like to sincerely thank the Ministry of Higher Education (MOHE) of Malaysia for the provision of a grant with code no FRGS01090010 to support this work. In addition, the supports and helps provided by all members of the Centre for Advanced Computational Engineering (CACE) at Department of Mechanical Engineering, UNITEN to carry out the research in this paper are deeply appreciated.

10. References

[1] D.B. Tuckerman, R.F.W Pease, "*High Performance Heat Sinking for VLSI*", IEEE Elect. Dev. Lett., vol. 2, 1981, pp 126-129.

[2] P.R. Parida, "*Experimental Investigation of Heat Transfer Rate in Micro-Channels*'', Master Thesis, Indian Institute of Technology Guwahati, India, 2007.

[3] I. Mudawar, "*Assessment of High Heat Flux Thermal Management Schemes*", IEEE Trans. Components and Packaging Tech., vol. 24, 2001, pp 122-128.

[4] S.G. Kandlikar, M.E. Steinke, "*Examples of Microchannel Mass Transfer Processes in Biological Systems*", in Proc. 1st Int. Conf. Minichannels and Microchannels, ASME, vol. 11, April 24-25, 2003, pp 933-943.

[5] K.C. Toh, X.Y. Chen, J.C. Chai, "*Numerical Computation of Fluid Flow and Heat Transfer in Microchannels*", Int. J. Heat Mass Transfer, vol. 45, 2002, pp 5133-5141.
[6] X.F. Peng, G.P. Peterson, "*Convective Heat Transfer and Flow Friction for Water Flow in Microchannels Structures*", Int. J. Heat Mass Transfer, vol. 39, 1996, pp 2599-2608.
[7] X.F. Peng, G.P. Peterson, "*The Effect of Thermofluid and Geometrical Parameters on Convection of Liquids through Rectangular Microchannels*", Int. J. Heat Mass Transfer, vol. 38, 1995, pp 755-758.
[8] I. Tiselj, G. Hetsroni, B. Mavko, A. Mosyak, E. Pogrebnyak, Z. Segal, "*Effect of Axial Conduction on the Heat Transfer in Microchannels*", Int. J. Heat Mass Transfer, vol. 47, 2004, pp 2551-2565.
[9] P.S. Lee, S.V. Garimella, D. Liu, "*Investigation of Heat Transfer in Rectangular Microchannels*", Int. J. Heat Mass Transfer, vol. 48, 2005, pp 1688-1704.
[10] J. Koo, C. Kleinstreuer, "*Laminar Nanofluid Flow in Microheat-Sinks*", Int. J. Heat Mass Transfer, vol. 48, 2005, pp 2652-2661.
[11] R. Chein, G. Huang, "*Analysis of Microchannel Heat Sink Performance Using Nanofluids*", Appl. Therm. Eng., vol. 25, 2005, pp 3104-3114.
[12] J. Lee, I. Mudawar, "*Assessment of the Effectiveness of Nanofluids for Single-Phase and Two-Phase Heat Transfer in Micro-channels*", Int. J. Heat Mass Transfer, vol. 50, 2007, pp 452-463.
[13] S.P. Jang, S.U.S. Choi, "*Cooling Performance of a Microchannel Heat Sink with Nanofluids*", Appl. Therm. Eng., vol. 26, 2006, pp 2457-2463.
[14] R. Chein, J. Chuang, "*Experimental Microchannel Heat Sink Performance Studies Using Nanofluids*", Int. J. Therm. Science, vol. 46, 2007, pp 57-66.
[15] T.H. Tsai, R. Chein, "*Performance Analysis of Nanofluid-cooled Microchannel Heat Sinks*", Int. J. Heat Fluid Flow, vol. 28, 2007, pp 1013-1026.
[16] S.E.B. Maiga, S.J. Palm, C.T. Nguyen, G. Roy, N. Galanis, "*Heat Transfer Enhancement by Using Nanofluids in Forced Convection Flows*", Int. J. Heat Fluid Flow, vol. 26, 2005, pp 530–546.
[17] S.V. Patankar, "*Numerical heat transfer and fluid flow*", Hemisphere Publishing Corporation, Taylor and Francis Group, New York, 1980.
[18] H.K. Versteeg, W. Malalasekara, "*An Introduction to Computational Fluid Dynamics*", The Finite Volume Method, Prentice Hall, London, 1995.
[19] R. Chein, J. Chen, "*Numerical Study of the Inlet/Outlet Arrangement Effect on Microchannel Heat Sink Performance*", Int. J. Thermal Sciences, vol. 48, 2009, pp 1627-1638.
[20] L.F. Moody, "Friction Factors for Pipe Flow", *J. Heat Transfer ASME Trans*, vol. 66 1944, pp 671-684.
[21] S. Kandlikar, S. Garimella, D. Li, S. Colin, M.R King, "*Heat Transfer and Fluid Flow in Minichannels and Microchannels*", Elsevier, USA, 2005.
[22] H.Y. Wu, P. Cheng, "*Friction Factors in Smooth Trapezoidal Silicon Microchannels with Different Aspect Ratios*", Int. J. Heat Mass Transfer, vol. 46, 2003, pp 2519-2525.
[23] H. Xie, J. Wang, T. Xi, Y. Liu, F. Ai, "*Thermal Conductivity Enhancement of Suspensions Containing Nanosized Alumina Particles*", J. Appl. Phys., vol. 91, 2002, pp 4568-4572.
[24] J.C. Maxwell, "*A Treatise on Electricity and Magnetism*", Clarendon Press, Oxford, UK, 1873.
[25] Y. Xuan, W. Roetzel, "*Conceptions for Heat Transfer Correlation of Nanofluids*", Int. J. Heat Mass Transfer, vol. 43, 2000, pp 3701-3707.

[26] A. Einstein, "*Investigations on the Theory of the Brownian Movement", Dover Publications*, Inc., New York, 1956.
[27] S.U.S. Choi, Z.G. Zhang, P. Keblinski, "*Nanofluids*", Encyclopedia of Nanoscience and Nanotechnology, vol. 6, 2004, pp 757-773.
[28] S.M.S. Murshed, K.C. Leong, C. Yang, "*Thermophysical and Electrokinetic Properties of Nanofluids-A Critical Review*", Appl. Therm. Eng., vol. 28, 2008, pp 2109-2125.
[29] D. Liu, S.V. Garimella, "*Investigation of Liquid Flow in Microchannels*", J. Thermophys. Heat Transfer, vol. 18, 2004, pp 65-72.
[30] C.J. Ho, L.C. Wei, Z.W. Li, "*An Experimental Investigation of Forced Convective Cooling Performance of a Microchannel Heat Sink with Al_2O_3/Water Nanofluid*", Appl. Therm. Eng., vol. 30, 2010, pp 96-103.
[31] D. Wen, G. Lin, S. Vafaei, K. Zhang, "*Review of Nanofluids for Heat Transfer Applications*", Particuology, vol. 7, 2009, pp 141-150.
[32] H. Xie, W. Yu, Y. Li, "*Thermal Performance Enhancement in Nanofluids Containing Diamond Nanoparticles*", J. Appl. Phys, vol. 42, 2009, pp 9-13.

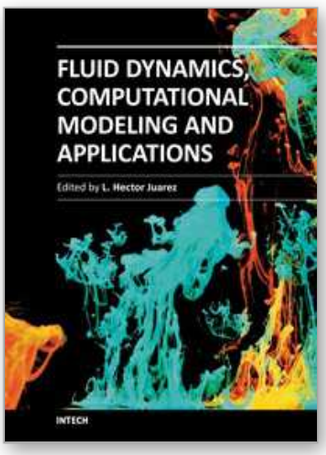

Fluid Dynamics, Computational Modeling and Applications

Edited by Dr. L. Hector Juarez

ISBN 978-953-51-0052-2
Hard cover, 660 pages
Publisher InTech
Published online 24, February, 2012
Published in print edition February, 2012

The content of this book covers several up-to-date topics in fluid dynamics, computational modeling and its applications, and it is intended to serve as a general reference for scientists, engineers, and graduate students. The book is comprised of 30 chapters divided into 5 parts, which include: winds, building and risk prevention; multiphase flow, structures and gases; heat transfer, combustion and energy; medical and biomechanical applications; and other important themes. This book also provides a comprehensive overview of computational fluid dynamics and applications, without excluding experimental and theoretical aspects.

How to reference

In order to correctly reference this scholarly work, feel free to copy and paste the following:

P. Gunnasegaran, N.H. Shuaib, H.A. Mohammed, M.F. Abdul Jalal and E. Sandhita (2012). Heat Transfer Enhancement in Microchannel Heat Sink Using Nanofluids, Fluid Dynamics, Computational Modeling and Applications, Dr. L. Hector Juarez (Ed.), ISBN: 978-953-51-0052-2, InTech, Available from: http://www.intechopen.com/books/fluid-dynamics-computational-modeling-and-applications/heat-transfer-enhancement-in-microchannel-heat-sink-using-nanofluids

INTECH
open science | open minds

InTech Europe
University Campus STeP Ri
Slavka Krautzeka 83/A
51000 Rijeka, Croatia
Phone: +385 (51) 770 447
Fax: +385 (51) 686 166
www.intechopen.com

InTech China
Unit 405, Office Block, Hotel Equatorial Shanghai
No.65, Yan An Road (West), Shanghai, 200040, China
中国上海市延安西路65号上海国际贵都大饭店办公楼405单元
Phone: +86-21-62489820
Fax: +86-21-62489821

IntechOpen